Components for micro-liquid handling and examples of hybridization in micro-systems

Dissertation
submitted to the Faculty of Sciences of the University of Neuchâtel
to obtain the degree of Doctor of science

by

Volker Gass

Ing.Dipl. Micr. EPFL

Institute of Microtechnology
University of Neuchâtel
Rue A.-L. Breguet 2
2000 Neuchâtel
Switzerland

printed by Imprimerie Moser SA
CH-2001 Neuchâtel

To Monique

And whatsoever ye do in word or deed, do all in the name of the Lord Jesus, giving thanks to God and the Father by Him.

col. 3:17

IMPRIMATUR POUR LA THÈSE

Components for micro-liquid handling and examples

of hybridization in microsystems

de M. Volker Gass

UNIVERSITÉ DE NEUCHÂTEL

FACULTÉ DES SCIENCES

La Faculté des sciences de l'Université de Neuchâtel sur le rapport des membres du jury,

Messieurs N. de Rooij, H. Hügli et P.A. Mäusli
(Mécanex Nyon)

autorise l'impression de la présente thèse.

Neuchâtel, le 31 octobre 1994

Le doyen:

H.-H. Nägeli

Abstract

The present thesis deals with the development of a flow rate sensor, to be included in Miniaturized Total Chemical Analysis System, μ-TAS, with the goal of controlling the flow rate of silicon micro pumps.

A variety of means to measure the flow rate of a liquid using miniature elements are shown. With the objective of using such a component in the environment described above, the different solutions are discussed briefly and one method is chosen.

A silicon micro pump which was manufactured in our institute by a novel technology is characterized and some of its strong and weak points highlighted.

A flow rate sensor has then been developed. After introducing the measurement principle, the manufacturing sequence is shown. The sensor is modelled using different approaches. The micro pump and the flow sensor were then integrated in a regulated system. An analytical approach to the regulated pumping system as well as practical results are shown.

During this thesis, some technological problems not related to fluid handling systems, were solved using the same or similar components as the flow sensor. The solutions are based on hybrid structures using silicon micro-sensors as sensing elements and conventional micro-mechanics as supports and interfaces. A micro-torque sensing system developed in partnership with MECANEX S.A. in Nyon Switzerland is shown. Another interesting application of a hybrid device used in the measurement of three-dimensional displacement of hip-bone implants in the human body is also presented.

Before concluding, several examples of applications of hybrid devices are shown.

Components for micro-liquid handling and examples of hybridization in micro-systems

0. Introduction

This chapter shows the frame in which the present work is placed. The motivation of the thesis is briefly explained, then it's structure is described.

The present work has been done under a project of the Swiss Committee for the Promotion of Applied Scientific Research (CERS) entitled "Development of a Miniaturized Total Chemical Analysis System (μ-TAS)", with as industrial partner CIBA-GEIGY Ltd, Basel, Switzerland.

The main elements of such a system are the fluid handling components and the chemical sensors. Such a μ-TAS using two silicon micro pumps had already been developed and presented by van der Schoot et al. in 1991 [1].

The present thesis deals with the development of a flow rate sensor, not included in the then existing μ-TAS, with the goal of controlling the flow rate of the existing micro pumps.

The first chapter shows a variety of means to measure the flow rate of a liquid using miniature elements. With the objective of using such a component in the environment described above, the different solutions are discussed briefly and one method is chosen.

The second chapter deals with the characterization of a silicon micro pump which was manufactured in our institute by a novel technology, giving rise to a patent. One of the most important drawbacks of such a pump is the dependence of the flow rate from the pressure difference between inlet and outlet.

The third chapter deals with the flow rate sensor as such. After introducing the measurement principle, the manufacturing sequence is shown. The sensor is modelled using different approaches and finally characteristics are measured and compared with theory.

The fourth chapter deals with the integration of the micro pump and the flow sensor in a regulated system. The analytical approach to the regulated pumping system as well as practical results are shown.

During this thesis, some technological problems not related to fluid handling systems, were solved using the same or similar components as the flow sensor. The solutions are based on hybrid structures using silicon micro-sensors as sensing elements and conventional micro-mechanics as supports and interfaces. This work is described in chapters five and six.

Chapter five deals with a micro-torque sensing system developed in partnership with MECANEX S.A. in Nyon Switzerland. This device allows absolute measurement of torque in, for instance, watch mechanisms.

Chapter six shows an interesting application of a hybrid device used in the measurement of three-dimensional displacement of hip-bone implants in the human body.

Before concluding, chapter seven shows examples of applications of the various devices.

1. Flow measurement

This chapter shows different means of measuring volumetric flow rate in liquids. The various characteristics are compared and one solution is chosen based on the application in a μ-TAS.

1.1 Introduction

Due to the increasing number of fluidic micro mechanical devices developed during the last 20 years, a development on component level [2,3] as well as system level [4,5,6] has stimulated the need to gain more information about the characteristics of the fluid flow. With this objective, various methods to measure volumetric flow or flow rate have been investigated.

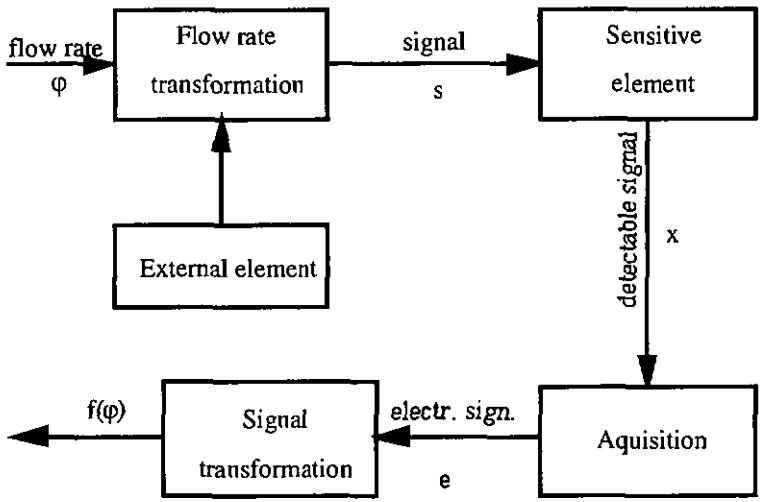

Figure 1 Flow rate measurement system

The objective of this survey is to identify a flow rate sensing principle to be used in liquid handling systems. One main goal is to achieve the regulation of a micropump that can be used for liquid handling systems such as needed in a μ-TAS [1].

In figure 1 the general schematic of a flow rate measurement system is shown. A volumetric flow, or flow rate, has to be transformed into a signal by an external element. A sensitive element placed in the stream yields a detectable signal. For example in a turbine, the external element is the wheel and its housing, and the senitive element is the encoder measuring the rotational speed of the turbine's shaft. The aquisition and signal transformation blocks modify the sensitive element's output into a convenient signal.

The various functions of this bloc diagram will be used in the present chapter as guide-lines for the description of the system. In a second stage, one of the sensing principles will be selected and the selection criteria discussed

1.2 Various principles using Microfabrication approach

A. Electrohydrodynamic flow meter

The electrohydrodynamic(EHD) micro flow meter was presented by Richter et al. in 1991 [7]. The EHD principle consists in generating a pulse of ions in the solution and measuring the transit time of this pulse between the generation electrode and a detection electrode placed downstream as shown in figure 2.

The exterior element, see figure 1, in this case is a step voltage which modifies the ionic concentration of the liquid. The ion concentration will be a function of the stimulation voltage. On the detection electrode, part of the generated ions are trapped and the current in the electrode varies as a function of the ion concentration. For a constant step voltage, the width of the ionic concentration pulse on the detection electrode is proportional to the liquid flow. A reference electrode is placed upstream of the pulse generation on the same device.

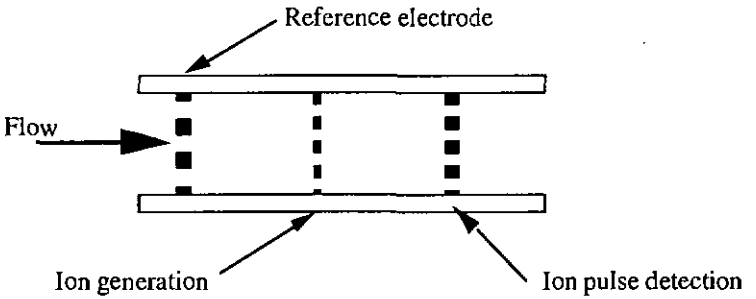

Figure 2 Schematic view of EHD flow sensor

After comparison with the current in the reference electrode and integration, a flow rate dependent signal is obtained. This is a third order function. The response time, ranging from 0.1 to 1 second, is proportional to the flow rate as a transit time is measured. With a distance of about 1 micrometers between excitation and detection electrodes, flow rates in the order of 1 micoliter per minute can be detected. This principle has been demonstrated by Richter et al. for flow rates down to 8 microliters per minute with a distance of 10 micrometers between the electrodes. The voltage applied was 300 volts at a frequency of 1 Hertz.

This solution allows a low detection limit by reducing the size of the device. However high voltages have to be generated and it has been observed that the voltage has to be adapted to the type of liquid used. The ionic concentration in the liquid is also affected by the measurement.

B. Hot wire anemometry

This method measures the heat dissipated through convection while cooling a resistor in a fluid flow as shown in figure 3 [3,8,9].

The exterior element transforming the flow rate into a detectable signal is the difference of electrical power required to maintain the heater-resistor temperature constant. When mounted in a Wheatstone bridge configuration with a second reference resistor, the voltage required to maintain the bridge voltage constant is proportional to the square root of the fluid's velocity.

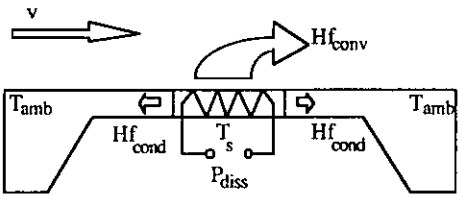

Figure 3 Schematic view of hot wire anemometer [39]

This element can be manufactured using classical or silicon technologies. It require a temperature difference in the fluid of at least 5 °C between the input and the output of the sensor so as to allow a good detection. The time constant of the device has been reported to be in the order of 100 milliseconds. Although this principle presents a precision of only about 10%, it has successfully been put on the market for applications in gas-flow measurements.

C. Thermal pulse detection

Closely related to the first solution presented, the generation and detection of a heat pulse in the fluid can also be considered. This principle has been presented by Branebjerg et al. in 1991 [10]. It consists in modifying locally the temperature of the liquid by sending a current pulse through a heating resistor placed in the flow channel.

This pulse is then detected downstream where the local temperature is monitored and constantly compared with a reference detector placed upstream. The measurement principle is shown in figure 4.

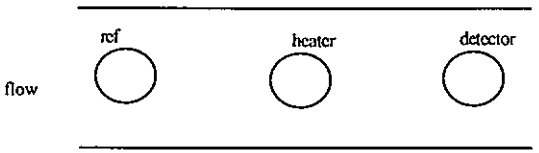

Figure 4 Heat pulse detection principle

Two modes of operation can be used to acquire the flow rate. The first consists in applying a single pulse and measuring the transit time between generation and detection. The second mode consists in a square wave excitation on the heater electrode and a determination of the phase-shift between excitation and detection. Both modes show a linear dependence between output signal and flow rate, this has been demonstrated by Branebjerg et al. for flow rates between 50 and 500 microliters per minute. The systems time constant is lower than 1 second in both modes. The measurement accuracy was 0.2% at full scale in the second mode of operation. Polar fluids could not be measured due to the EHD effect discussed earlier.

D. Interferometric lift-force detection

An obstacle placed in the fluid flow will be subject to a drag force, parallel with the direction of the flow, and a lift force perpendicular to the direction of the flow [11]. These forces are due to the pressure differences around the obstacle which are induced by the flow of the fluid.

If, as shown in figure 5, the obstacle were to be part of an optical Fabry-Perrot cavity, the displacement of the obstacle due to the flow velocity could be detected by optical interferometry. No publication integrating interferrometry and lift force have been found.

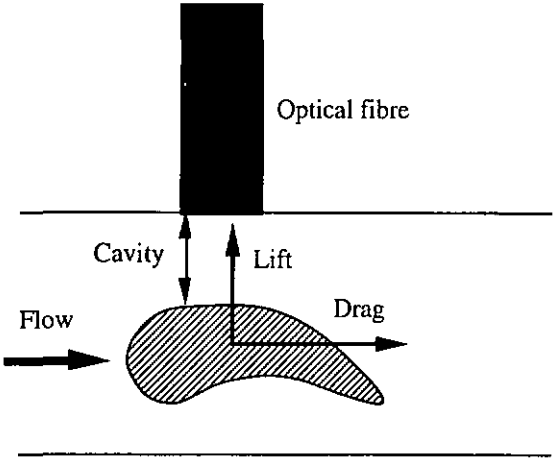

Figure 5 Principle of interferrometrical detection

In the present case, the wavelength of the signal reflected from the F-P cavity is modulated as a function of the cavity's optical length. The output signal of the sensor is extremely non-linear and requires computer assistance in its treatment. Results using this type of detection principle by Hälg et al. [12] show that displacements from 1 nanometer to 3 micrometers have been detected.

This method has the advantage of no-contact. However the geometrical accuracy has to be guaranteed to ensure correct functioning. Changes in refraction index of the fluid are not allowable prior to re-calibration of the device.

E. Piezoresistive drag-force detection

The force parallel to the fluid flow acting on an obstacle (drag force) can be detected by measuring the stress induced by the fluid's velocity in the elastic suspensions of the obstacle. This principle was demonstrated by Schmidt et al. in 1987.[13] The principle of operation is shown in figure 6.

Again the difference in pressure between the upstream and downstream sides of the obstacle is proportional to the fluid's velocity. This principle was tested in our laboratory using a cantilever-type accelerometer[14] placed into the fluid stream.

Depending on the ratio between the dimension of the obstacle perpendicular to the direction of the flow and the dimension parallel to the direction of the flow, two models can be used. If the ratio is low, the pressure drop depends on the length of the obstacle [13] and the phenomenon is called skin-friction drag. If the ratio is high, the pressure drop depends on its surface perpendicular to the flow [14] and the phenomena is called restrictive drag.

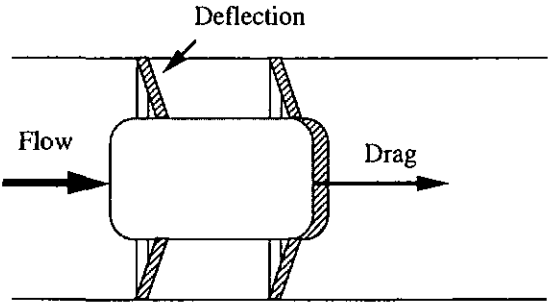

Figure 6 Drag force measurement principle

The seismic mass of the cantilever acts as obstacle and piezo-resistors diffused in the mass suspensions can detect its deflections. Tests were conducted with silicon oil and flow rates in the tens of nanoliter per minute range were detected. For low flow rates, as long as the flow is laminar, the response of the device is linear. Time constants independent of the flow and lower than 1 millisecond were observed.

F. Rotary element detection

A miniature wheel or turbine placed in the fluid stream will be actuated if the fluid is directed onto its edge, as shown in figure 7. This has been demonstrated by Field et al. for rotary gears driven by water [15].

The rotation speed is proportional to the speed of the fluid. Detection of the rotary speed can be done via an optical fibre as demonstrated by Bley et al. in 1991 [16].

The main problem is to overcome the friction by high fluid velocity. For example Field et al. showed that the forces opposed to the movement are in the same order of magnitude as the driving force. Water would have to flow at a velocity of about 0.2 meters per second to overcome these opposing forces. This means a flow rate of 200 microliters per minute in a channel of 40 by 40 micrometers.

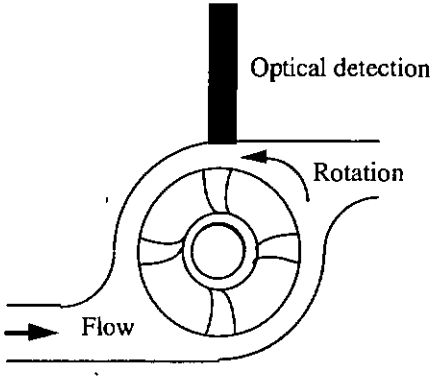

Figure 7 Rotary actuation and detection principle

1.3 Selection of principle

If we consider the application for the flow rate sensor to regulate a micro pump for a µ-TAS, the following conditions have to be met.

The fluid used is an incompressible aqueous solution that has to be kept at constant temperature. The ionic concentrations of the liquid must not be modified during sensing. The micropump, as will be shown in chapter 2, operates between 0 and 500 microliters per minute with water or an aqueous solution. To be able to regulate this flow between 10 and 100 microliters per minute, the detection limit should be around 1 microliter per minute.

The comparison between the different solutions on a performance basis is shown in table 1. Only the last three solutions do not interact with the liquid in terms of temperature and ionic concentration. The rotation drive requires high liquid velocities and the operating life of such a device is reduced by the wear of the wheel's axis. Interferrometrical detection of drag or lift force remains a very interesting solution although this technology presents a high risk as all dimensions in the F-P cavity have to be perfectly aligned.

The solution chosen is the piezo electric detection of the stress induced in the obstacle's suspensions due to the force exerted by the fluid flow. The technological risk is small and preliminary tests with silicon integrated accelerometers show that the specified detection limit can be reached.

Three functional models were manufactured during the end of 1991 using existing piezo-resistive cantilever accelerometers, developed in our institute by T.Tschan [14]. When mounted into a fluid stream, the seismic mass of the accelerometers was deflected causing a variation of the measuring bridge's output. This measurement principle was also demonstrated in gases by van der Wiel et al. [38].

These functional models worked only with insulating fluids such as silicon oil, as the resistors are diffused directly into the surface of the beam. Liquids such as water or aqueous solutions create a short-circuit making the measurements impossible.

When pumping silicon oil having a relative viscosity to water of 96, the sensitivity of the sensor without amplification was about **20 µV/µl/min**.(direct output of the bridge powered by 1 VDC)

These results allowed the optimisation of a prototype series of sensors, dedicated to the measurement of flow-rates in other liquids such as water.

Table 1 Performance comparison of flow-rate sensor solutions (A = EHD, B = Hot Wire Anemometry, C = Thermal Pulse, D = Interferometric lift-force, E = Piezoresistive Drag-force, F = Rotary Element)

Evaluation
++ / + / 0 / - / --
good —> bad

SOLUTIONS

CRITERIA	A	B	C	D	E	F
Transformation of flow rate	ΔC ions -	ΔP dissip. 0	ΔT impuls +	ΔX obst. ++	ΔX obst. ++	ΔX' rotat. +
Type of signal	I ions 0	I therm +	phase shift 0	wave-len. 0	stress ++	rotation +
Sensitive element	ISFET 0	resistor ++	resistor ++	Phot. dio +	resistor ++	phot diode +
Type of detectable signal	Δt peak I -	ΔI{loss} +	Δt wave 0	Δλ interf. 0	ΔR piezo ++	Δ frequ. +
Output characteristic	order 3 +	order 0,5 +	linear ++	spiral –	linear ++	linear ++
Response time	0,1 sec 0	0,1 sec 0	1 sec -	< msec ++	1 msec +	> msec +
Technical complexity	high -	average 0	average 0	high --	simple ++	simple ++
Price Technology	- 0	+ +	0 +	-- --	++ 0	- -
Global eval.	**Average**	**good**	**good**	**Risk**	**v. good**	**average**

1.4 Conclusion

The flow rate sensor principle chosen is the piezo-resistive detection of the stress induced by the force parallel to the direction of the flow. This concept is promising as it can fulfil the specifications and the technological complexity allows easy manufacturing in a standard silicon manufacturing line.

The proposed solution is a cantilever beam placed in a fluid flow. At the end of the beam the fluid passes through an orifice. Strain gages on the extremity of the beam measure the stress caused by the deflection of the beam. In the chosen geometrical configuration the stress is directly proportional to pressure drop over the orifice.

The stress is measured via an integrated piezo-resistive Wheatstone bridge. All resistors are diffused simultaneously close to each other to minimise offset and electrical noise when measuring.

The advantages of this configuration are:

- Flow measurement without complex signal handling is possible.
- High sensitivity can be achieved by adapting the geometry.
- Low response time.
- No modification of physical flow parameters.
- All fluids can be detected if the measurement resistors are isolated.

2. Micropump characterization

This chapter deals with the characterization of the improved micropump developed at the Institute of Microtechnology, Neuchâtel, Switzerland. Its characteristics will complete the requirement for the flow rate sensor.

2.1 Introduction

In 1980, a peristaltic piezoelectric fluid pump was developed at Stanford University by Smits [17] and several prototypes were realized in silicon wafers. Since 1983 research has been carried out at the University of Twente on the possibility of realizing a micropump based on micromachining of silicon and thin-film technology [18,19]. These pumps have been shown to yield flow rates up to several tens of microliters per minute. The maximum pressure build-up is several hundreds of millibar at zero flow [20,21,22,23].

The design of the micropump presented hereafter is similar to that of van Lintel et al. [18]. It consists of a micromachined silicon part anodically bonded between two pyrex glass plates. The thicker glass plate (1.5 mm) serves as the base plate for the fluid connections. The thinner glass plate (0.3 mm) forms the pump membrane that is driven by a piezoelectric disc (Philips PXE 5, silver electrode, 10 mm diameter, 0.2 mm thickness). The actuator disc is cemented to the thinner glass plate using conductive epoxy. Micromachining of the silicon chip forms two passive valves against the glass base plate.

Figure 8 shows a cross section of the pump and explains its operation. The actuator is driven with a square wave voltage with an amplitude up to several hundred volts. The maximum pump rate is obtained at a frequency of 40 Hertz and is in the order of 500 µl per minute. The maximum pressure build-up is 300 millibar at zero flow.

At rest, both the inlet and the outlet valve are closed and no liquid is flowing. When a voltage is applied to the piezo disc, the glass membrane bends downwards, increasing the pressure in the chamber. The liquid is then forced though the normally closed outlet valve. As the voltage drops again, the pressure in the pumping chamber drops, sealing the outlet valve and opening the inlet valve thus filling the pumping chamber. Finally the pressure difference across the inlet valve equals out and the original condition is regained.

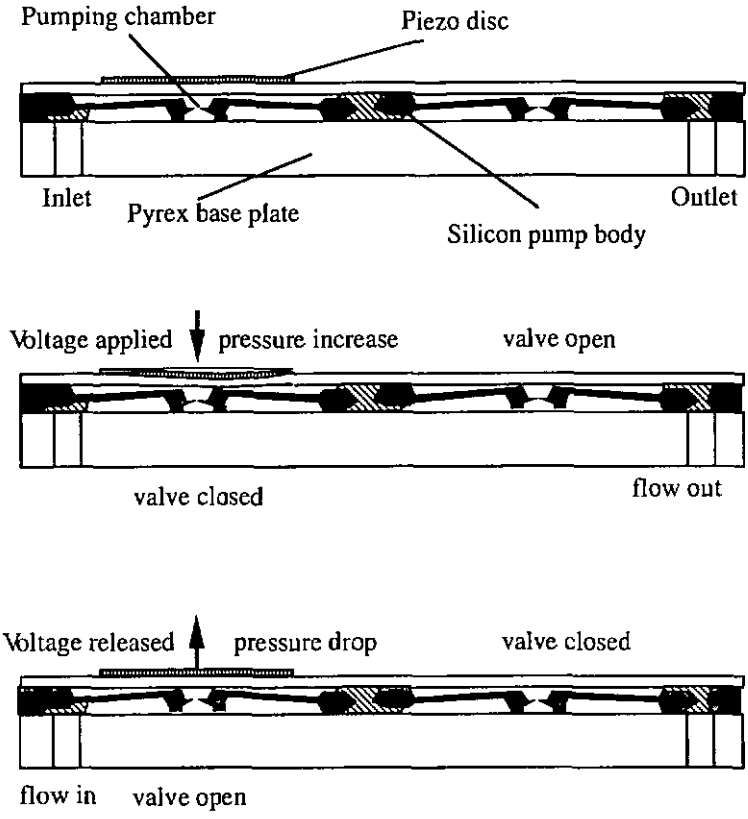

Figure 8 Cross section of the piezoelectrically driven micro pump

2.2 Description of micropump

General design characteristics have been described in detail and will not be repeated here [18]. The pump dimensions are the following:

Dimensions	value (mm)
Chip size	22 x 22
Pump membrane diameter	12.5
Valve diaphragm diameter	7
Pump chamber depth	0.115
Sealing ring inner & outer diameter	1.2 &1.5
Valve membrane thickness	0.050
Oxide film thickness	0.001

Table 3 Micropump dimensions

One of the main problems of silicon liquid handling components is that silicon is hydrophobic. This makes the filling or priming of such a micropump difficult. One solution is to "wet" the pump with alcohol, another is to coat the pump's surface with a hydrophilic layer. The manufacturing process described hereafter has made the object of a patent application [24]. It allows selective in-process coating of the flow channels in order to improve the pump's overall performances.

The manufacturing sequence is a fairly simple 4 mask process. The main steps are the top-side pre-etch of 50 µm which determines the membrane thickness, see figure 9, and the double sided "deep" etch which will liberate the structures.

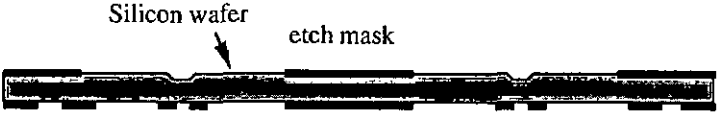

Figure 9 Mask deposition prior to deep anisotropic etch

The etch mask remains in place only on the valve seats. This ensures that the valves do not stick to the base plate during the anodic bonding (figure 10). The hydrophilic coating is applied prior to the encapsulation. The piezo-disc is the cemented in place and the whole pump mounted in a fixture that allows for both electrical and fluid connections.

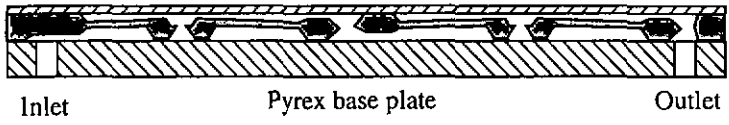

Figure 10 Pump after etch and anodic bonding of pyrex plates

The pump fixture was designed for use inside a space bioreactor [25]. It consists of polyimide base plate accommodated with a surgical needle at its input and a threaded hole for the output connection. Two o-ring seals ensure for water tightness. This type of fixture allows simple replacement of the pump, should the need arise.

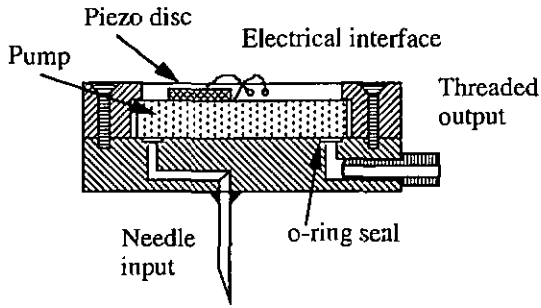

Figure 11 Mounted micropump

2.3 Characteristics

As described earlier, the pumping chamber's volume is modified upon applying a voltage to the piezo-disc.

The voltage causes a radial contraction of the piezoceramic disc and the resulting moment of flexure forces the thin glass membrane to curve inwards, hence a difference in volume in the pumping chamber.

Measurement set-up

As shown in figure 12, the measurement set-up consists of a set of driver electronics generating the high voltage, a reservoir filled with filtered liquid, a micropump, a high precision micro-balance and a computer assisted readout transforming the mass variations into flow rate in real time.

The differential pressure between the input and output of the total system is zero. In the present case the reservoir and balance are at the same height as the pump. The only pressure drop due to the system itself, tubing & channels, has to be compensated by the pump.

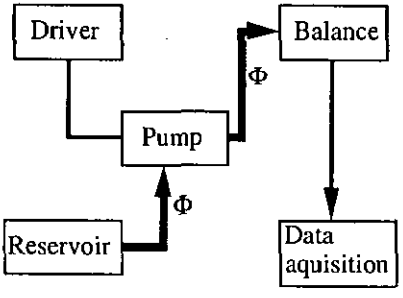

Figure 12 Measurement set-up

It is to be noted that one of the limitations of the present driver electronic configuration is the drop in efficiency at frequencies over 50 hertz. The capacitor-diode cascade does not react fast enough at these frequencies and the square wave voltage desired is altered significantly, as shown in figures 13a & 13b.

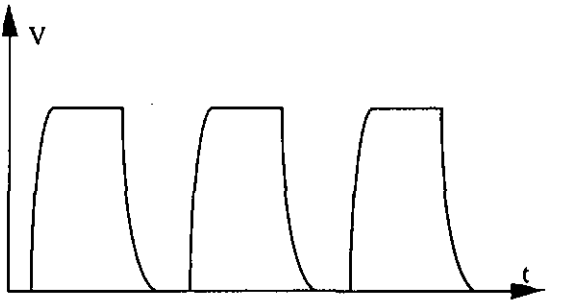

Figure 13a Driver output at low frequency

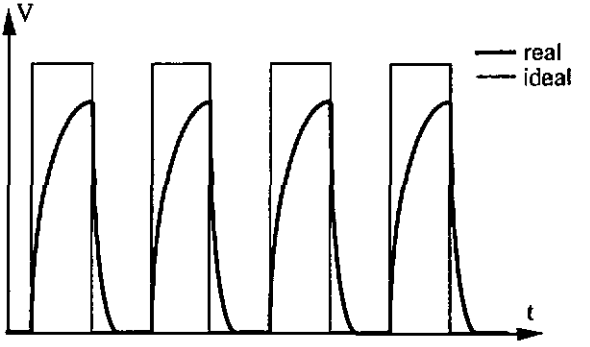

Figure 13b Driver output at high frequency

Results

Measurements were conducted in laboratory conditions so as to determine the pumps response with respect to actuation voltage and actuation frequency. The effect of the degradation of the actuation signal as shown in figure 13 can be seen in figure 14.

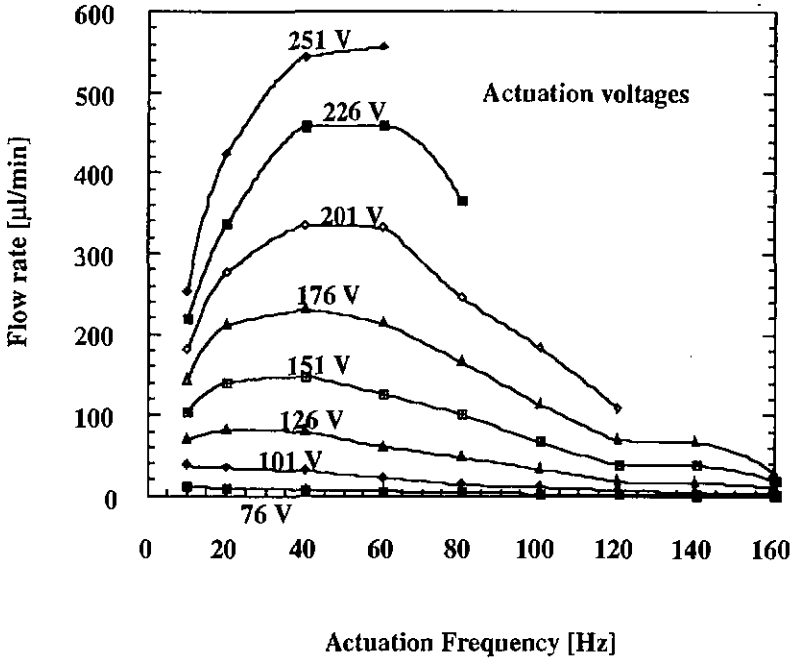

Figure 14 Micropump flow rate vs. actuation frequency

For this reason the actuation frequency is chosen to be 40 hertz. The flow rate versus voltage characteristic is shown in figure 15 for a 40 hertz actuation frequency and flow rates between 0 and 500 microliters per minute.

As described by van Lintel et al. [18] a certain voltage (pressure) is required to overcome the pre-tension of the valves. At low frequencies the complete volume is pumped out before the pressure is released. Thus at low actuation frequencies, the flow rate is proportional to the actuation frequency.

The pump is now coupled to a flow sensor(described in chapter 3) which allows to study the detail of each stroke (figures 16 and 17). Such a single stroke is represented in figure 16 under a frequency of 0.9 Hertz and an actuation voltage of 150 volts.

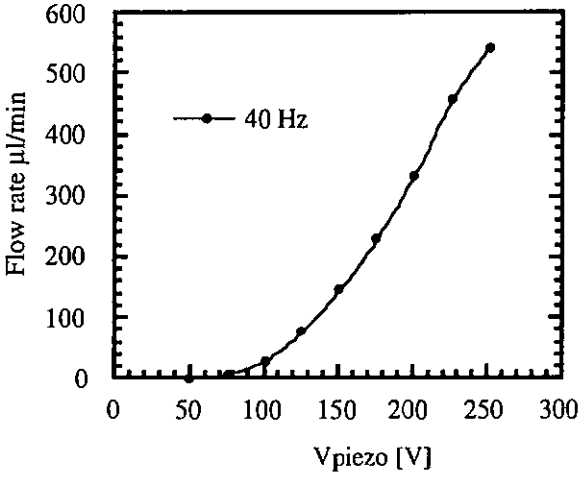

Figure 15 Flow rate characteristic at 40 hertz

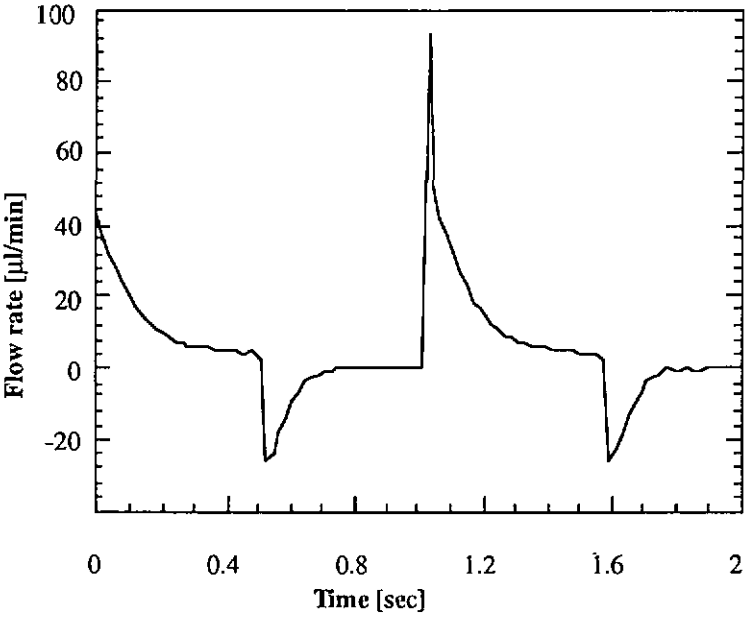

Figure 16 Pump flow rate at 0.9 Hertz actuation frequency

The volume pumped is proportional to the integral of the flow rate over time. We can observe a slight back-flow as the voltage on the piezo disc is released. Most of the liquid passes through the pump during the first 200 milli-seconds. This means that at higher frequencies and voltages only the more "efficient" part of the stroke will actually contribute to the pumping.

The back flow shown in the example above is always present due to the closing motion of the valves. However, bad sealing of the pump's valves will greatly increase this phenomena.

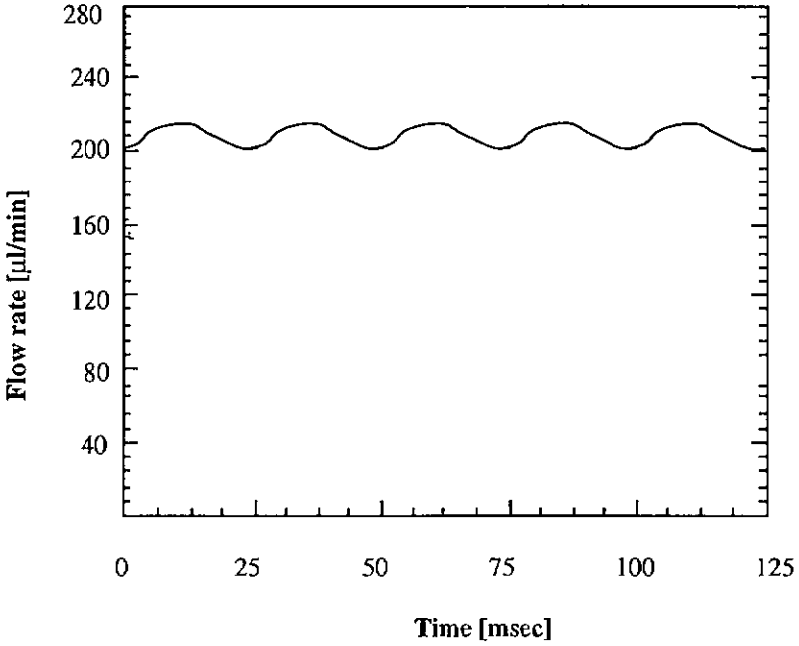

Figure 17 40 Hertz actuation frequency at 170 volts

At 40 Hertz for example, see figure 17, the flow rate profile is close to a sine wave with a positive offset. This means that the inertia of the liquid and of the valves does not allow any back flow and the average flow rate is greatly increased.

One of the main disadvantages of the pump presented here is the strong dependence of the output flow rate with respect to a pressure difference between inlet and outlet. This characteristic is represented in figure 18.

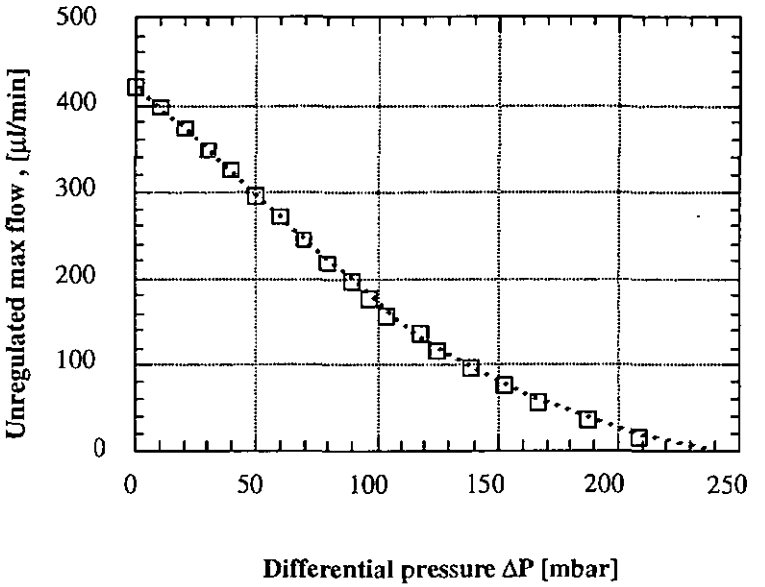

Figure 18 Pump output versus pressure difference between outlet and inlet of the pump at 200 volts / 40 Hertz actuation

From figure 18 we can see that the maximum pressure build-up is about 250 millibar at zero flow for an actuation voltage of 200 volts at 40 Hertz.

2.4 Conclusion

The micropump is one of the most important components used in micro liquid handling, hence the wide interest in many research groups. However, the use of silicon technology also has a few major drawbacks. Filling and priming are relatively complicated even after the pump has been coated as described. Small gas bubbles will tend to get stuck in he channels reducing the pump efficiency. Particle contamination, even for particles smaller 1 micrometer in diameter, will cause leakage through the valve seats and also result in a drop in efficiency. These aspects will not been described here and the fluid pumped is considered filtered and outgased. The pressure dependence of the micropump agrees with the modelization done by van Lintel et al. [18]. This is the effect that will be compensated by regulating the pump's flow, as will be described in the following chapters.

3. Flow-sensor

After having described the the micro pump, we come to the main part of this thesis. The present chapter deals with the drag-force micro flow-sensor developed for fluid handling systems [26]. The sensor will be presented, different models discussed and the practical results shown.

3.1 Introduction

The drag on an object immersed in a liquid flow is comprised of two components: skin-friction drag and restriction drag [27]. Depending on the situation either one of the two can be the predominant one. This is illustrated in figure 19:

- A thin plate placed parallel to the direction of a flow, as in figure 19a, gives little disturbance to the flow, but induces a shear stress in a boundary layer adjacent to the surface. In this situation the skin-friction drag in predominant.
- A thin plate placed perpendicular to the direction of a flow, as in figure 19b, has a small boundary layer, but will cause a significant disturbance to the path of the flow. In this situation the restriction drag is predominant.

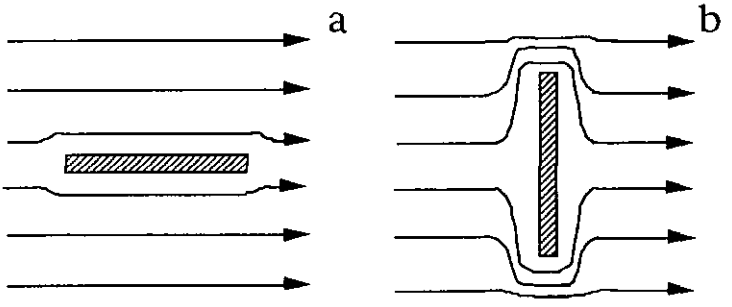

Figure 19 A thin plate placed in a liquid flow with an optimal skin-friction drag (figure a), and with an optimal restriction drag, (figure b).

The cantilever of the flow sensor is however not placed in an infinite fluid, but is a system of a short flow channel at the end of a cantilever. The viscous friction on the flow channel walls creates a pressure difference that acts on the cantilever.

This pressure difference can be calculated using two different approximations as described later. The force from the skin-friction drag on the cantilever end and the force from the restriction drag.

The pressure difference causes a momentum in the thinner suspension of the cantilever, this momentum causes a surface stress that is detected by piezo resistors doped in the surface of the suspension.

3.2 Manufacturing

The flow sensor consists of a cantilever liberated from a two level membrane etched in silicium (profile shown in figure 24). The thicker region of the membrane (≈ 50 µm) is under the cantilever, the thinner regions (≈ 20µm) is along the edges of the liberated cantilever and under the fixed end, where the bending is to be concentrated. On the upstream side of the cantilever, over the bending part, four piezo resistors are doped into the surface. These piezo resistors are connected to aluminium contact pads by highly doped conductors.

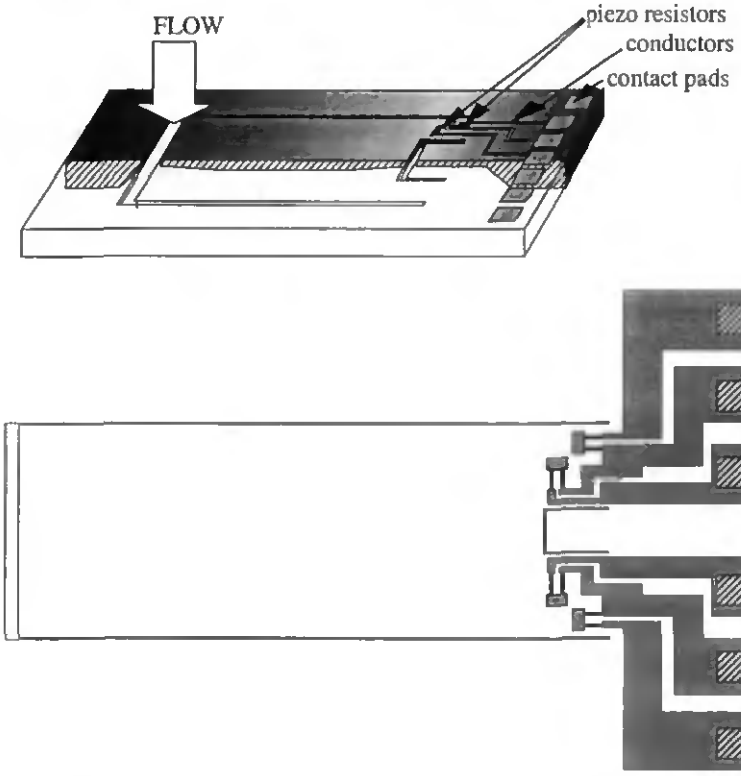

Figure 20 Flow sensor lateral and top detail view.

The manufacturing process is divided into four phases: doping of the resistors and conductors on the component side, etching of the two level membrane from the cavity side, deposition of the aluminium contact pads and a plasma etch liberating the cantilever from the membrane.

The doping of the resistor and conductors is done by diffusion from doped oxides. Three 1000 Å layers of doped oxide are deposited on top of each other, separated by two 4000 Å layers of undoped oxide. Each oxide contacts the bulk silicium where the doping from the oxide is wanted. These oxides are shown after the diffusion in figure 21.

The first oxide is strongly phosphorus doped and defines a channel stop region covering the whole chip. The channel stop also serves as an ohmic contact to the n-type bulk material, thus forming a diode under the resistors and conductors to minimise leakage currents. The second oxide is boron doped and defines the piezo resistors. Using **mask Nº 1** contact windows are etched through the first oxide and the undoped protection oxide. The third oxide is strongly boron doped and defines the conductors from the resistors to the aluminium contact pads, using openings defined by **mask Nº 2.**

After the deposition the impurities are diffused into the bulk silicium at 1100 °C in 50 min, and the oxides are removed.

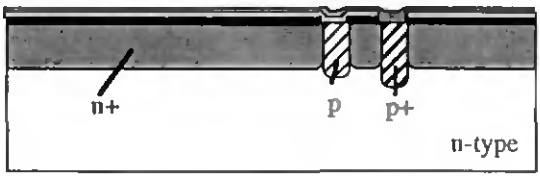

Figure 21 The three doped oxide layers on the component side after the diffusion before the oxides are removed.

The etching of the two level membrane from the cavity side is defined by one protective oxide and two nitride masks deposited and defined on top of each other, before the exposure to the KOH etch. This process also leaves a protective layer over the piezo resistors on the component side.

First a 2000 Å protective oxide is deposited on both sides. On top of this a 1900 Å nitride is deposited and plasma etched on both sides to define the unetched parts of the cavity side and the resistor protection on the component side. This uses **masks N⁰ 3 and N⁰ 4.** On top of this a second 1900 Å nitride is deposited on both sides. This layer is etched on the cavity side to define the thinner regions of the membrane, using **mask N⁰ 5.** These layers are shown in figure 22.

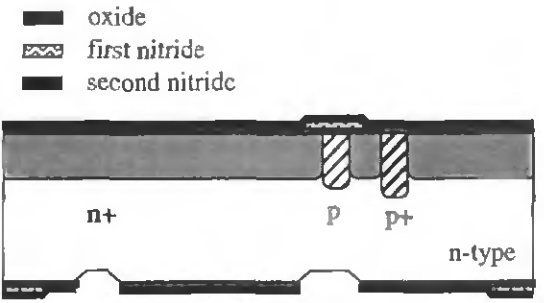

Figure 22 The one oxide and two nitride layers on both sides defining the channel and the resistor protection. The layers are shown after the first KOH etch, before the plasma etch removes the last deposited nitride.

The technique of defining the two nitride layers on top of each other before any KOH etching is done, is used because it is not possible to spin the mask resist over the cavities left by the first KOH etching. With this technique the last deposited nitride is removed after the first KOH etch by a uniform plasma etch, leaving the first deposited nitride.

The openings in the last deposited nitride mask is BHF etched into the protective oxide and then anisotropically KOH etched 40 µm into the bulk silicium. The first deposited nitride mask is then uncovered, BHF etched into the protective oxide and KOH etched. This mask frames the cavity, and the edges have only (100) and (111) planes exposed during the etch. The middle plateau is exposed from all sides yielding a concave profile due to the different etch -rates in the different orientations, this is shown if figure 23.

- bulk silicium
- first deposited nitride, defining the cavity walls
- second deposited nitride, defining the thinner membrane regions

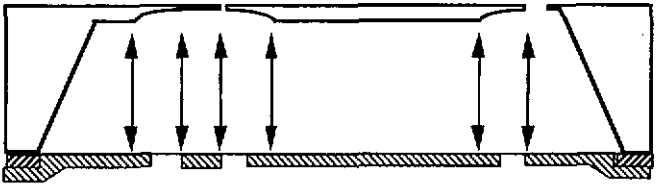

Figure 23 The two nitride masks and the final KOH etch result.

After the KOH etch, the last deposited nitride on the component side is removed by plasma etch leaving the first deposited nitride and the protective oxide as a protection over the resistors.

The definition of the aluminium contact pads is done by a uniform deposition and an etch using mask N° 6.

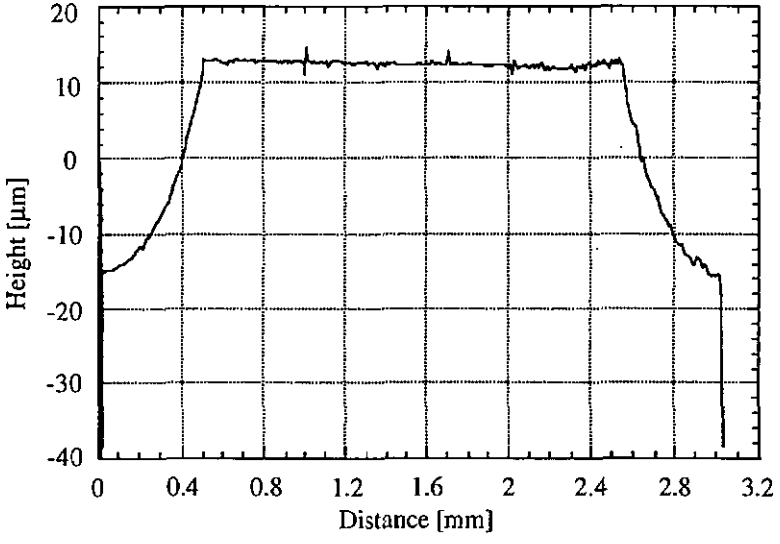

Figure 24 Scan along the centre of the cantilever backside.

The selective plasma etch liberating the cantilever and creating the main flow opening uses mask N° 7.

In figures 24 and 25, the backside profile is shown. It is important to note that the beam thickness increases gradually. This has to be taken into account for the modelization of the sensor as will be seen later.

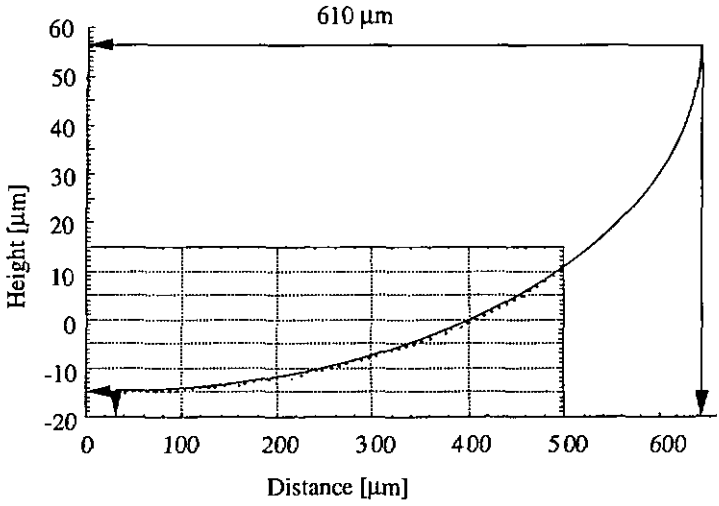

Figure 25 An ellipse fit to the cantilever scan in figure 25.

In Table 2 the geometrical dimensions of the sensor as well as the physical parameters considered for the following modelizations are given.

Table 2 Flow-sensor geometrical considerations

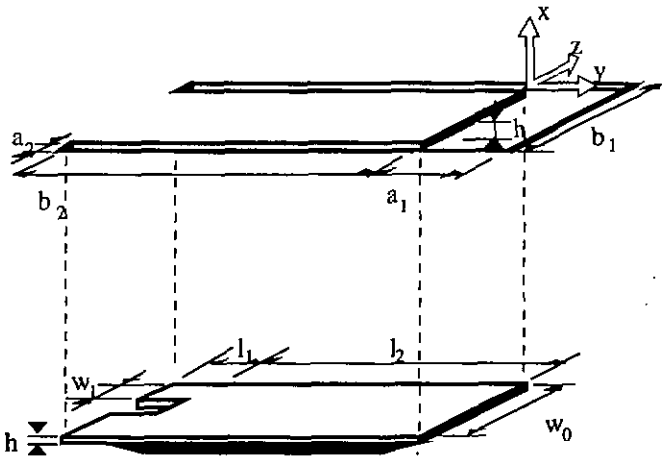

Geometrical Measurements: dimensions in meters

$a_1 = 30.0\ 10^{-6}$	$a_2 = 10.0\ 10^{-6}$	$b_1 = 1000.0\ 10^{-6}$
$b_2 = 3000.0\ 10^{-6}$	$h = 20.0\ 10^{-6}$	$l_1 = 300.0\ 10^{-6}$
$l_2 = 3000.0\ 10^{-6}$	$w_0 = 1000.0\ 10^{-6}$	$w_1 = 400.0\ 10^{-6}$

Physical parameters:

A	cross-sectional flow area	$30\ 10^{-9}\ m^2$
A_{End}	area of cantilever end	$20\ 10^{-9}\ m^2$
A_{Cant}	area of cantilever perpendicular to the flow	$3\ 10^{-6}\ m^2$
C	constant, Ref.[b]	96
D_h	hydraulic diameter 4A/wetted perimeter	
	end:	$58\ 10^{-6}$ m
	side:	$20\ 10^{-6}$ m
E	Young's modules	$169\ 10^9\ N/m^2$
Q_V	volumetric flow, at 100 µl/min	$16.7\ 10^{-10}\ m^3/s$
µ	viscosity, (water, 20 °C)	10^{-3} kg/ms
ρ	density, (water, 20 °C)	$10^3\ kg/m^3$
υ	Poisons ratio	0.42

Formula parameters:

I	moment of inertia,	$[m^4]$
K_{GI}	gauge factor	
$M_{\Delta P}$	moment from the pressure difference on the cantilever,	[Nm]
M_R	moment from the restriction dragon the cantilever	[Nm]
M_{SF}	moment from the skinfriction on the cantilever	[Nm]
p	pressure difference,	$[N/m^2]$
ΔP	total pressure difference over the cantilever,	$[N/m^2]$
Re	Reynolds number	
U	average speed of the fluid,	[m/s]
u	speed of the fluid,	[m/s]
x, y, z	co-ordinates	[m]
π_l	long. piezores. coef.	$[m^2/N]$
π_t	trans. piezores. coef.	$[m^2/N]$
σ	stress in beam	$[N/m^2]$
τ	shear stress,	$[N/m^2]$

3.3 Modelling.

Flow in the sensor

For an internal flow passing an obstacle there are three zones of flow.

- Laminar flow, which is constant in time and which will show the same flow lines if the flow is reversed.
- Eddy flow, which is constant in time but includes back flow eddies. If the flow direction is altered, the flow lines will change.
- Turbulent flow, which is not constant in time.

The flow lines for the three types of flow are illustrated in figure 26.

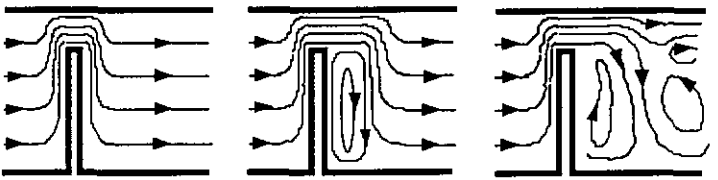

Figure 26 The flow lines for laminar flow, eddy flow and turbulent flow respectively.

The laminar flow in the sensor is a very important assumption for the modelizations. The path lines of the flow were therefore determined to prove the laminar flow.

"A path line is the path or trajectory traced out by a moving fluid particle " [11].

The experimental set-up was a special mount of a flow sensor under a LCD video camera. The flow sensor had been sawn to make the flow channel visible. It was then glued on a glass plate and the liquid connection was build up by plastic tubes. This is shown in figure 27.

The output from the video camera was treated by computer using the application programs Adobe photoshop 2.0 and Imagegrabber 2.1.

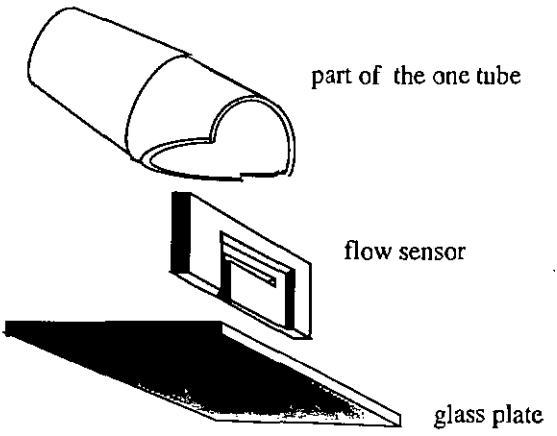

Figure 27 Mounting of a cut flow sensor to obtain the flow path lines.

Two types of images were obtained:

- Water-isopropanol interface patterns on the glass surface were seen due to the different diffraction of the backlight through the two liquids. This effect was only observable at high flows (>800 µl/min) because the two liquids would mix at lower flows, also surface effects on the glass could be important at flows with less kinetic force. Figure 28 shows flow patterns recorded at about 1000 µl/min. The sensor opening can be seen on the left hand side.

- Thus colored water was injected close to the cantilever opening (≈1mm). The solution was injected this close because of the fast dilution. The syringe tip used for the injection was placed in the middle of the flow channel to avoid the effect from the opening between the cantilever side and the glass. The camera was then focused on the syringe tip and thus on the flow path.

  A sodium permanganate solution was observed passing the cantilever at 230 µl/min. The flow was seen on the video recording to be clearly laminar.

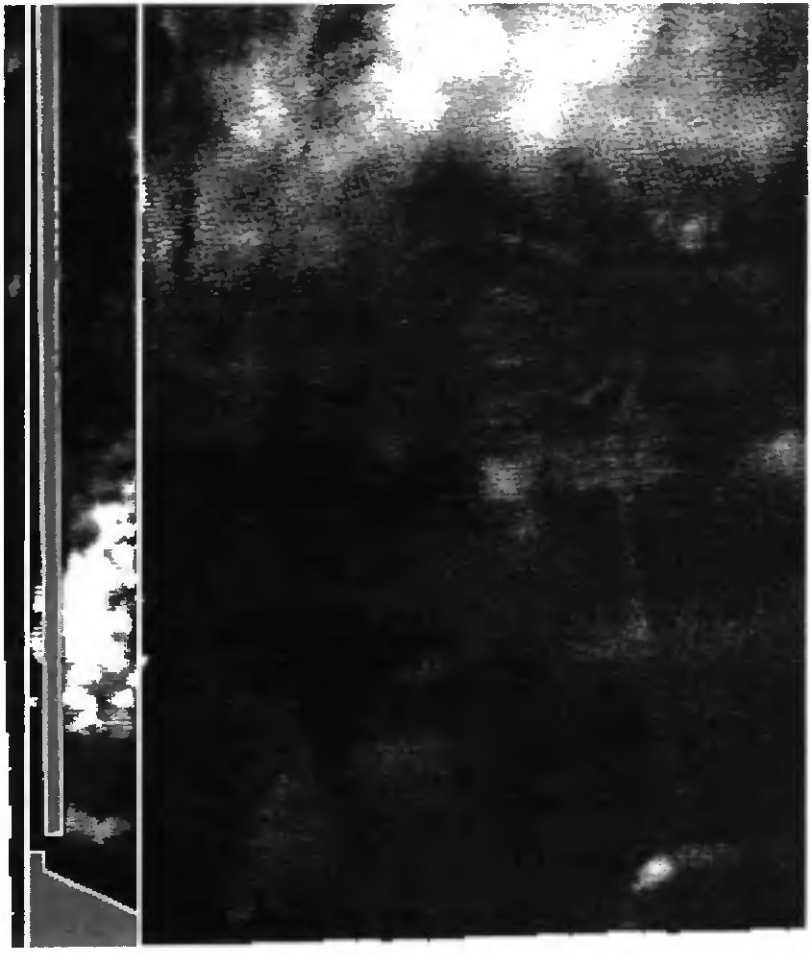

Figure 28 Flow pattern with eddy flow at 1000 µl/min. Sensor opening is shown on left hand side and eddy can be seen in the center.

The following modelization considers the conributions of the two types of drag-forces shown in figure 19.

First model: Pressure difference due to restriction drag

The first model is based on the pressure drop in an equivalent circular flow channel [26].

The assumptions for the first model are that the flow of an incompressible fluid is laminar and dominated by viscous forces. Further more, the ratio between the channel length and the hydraulic diameter must be less than 0.5 [27]. Tables 3 & 4 give the models for flow in small channels as a function of channel geometry and Reynolds numbers.

Table 3 Flow models for incompressible liquids at various Reynolds numbers [27]

Type of restriction	Definition	Viscous losses dominate laminar flow (Re<<Re_t)	Re_t
Orifice	$L/D_h<0.5$	$Q_v = A \frac{2}{C} \frac{D_h}{\mu} \Delta P$ (1)	15
Short channel	$2<L/D_h<50$	$Q_v = A \frac{2}{C} \frac{D_h^2}{L\mu} \Delta P$ (2)	$30L/D_h$
Long channel	$L/D_h>100$		2300
Diffuser inlet (D_h') outlet (D_h) (A is the smallest area)	$5>L/D_h>50$	$Q_v = A \frac{6}{C} \frac{D_h^2}{L\mu} \frac{\left(\frac{D_h^3}{D_h'^3} - 1\right)}{\left(1 - \frac{D_h'}{D_h}\right)} \Delta P$	$30L/D_h$

Table 4 Definition of parameters

A	Cross sectional area of flow path
D_h	Hydraulic diameter $\left(\frac{4\ A}{\text{wetted perimeter}}\right)$
L	Length of channel in flow direction
C	Friction coefficient: (= f·Re)
	= 64 for circular cross section
	= 96 for rectangular cross section (w >> h)
f	Pressure loss coefficient
	Friction factor ($\approx 0.14 \cdot Re^{-0.18}$ for fully developed turbulent flow)
P_{in}	Inlet pressure
P_{out}	Outlet pressure
ΔP	= P_{in} - P_{out} ; pressure drop
Q_v	Volumetric flow at output
µ	Dynamic viscosity
ρ	Fluid density
U	$= \frac{Q_v}{A}$;Average fluid velocity
Re	$= \frac{U\ D_h\ \rho}{\mu}$; Reynolds number
Re_t	Transitional Reynolds number

- The fluids, water or aqueous solutions, can be considered quasi-incompressible since the normal working pressure does not exceed 200 mbar.

- The flow is laminar because the Reynolds number is lower than the transitional Reynold's number Re_t. We have at a volumetric flow of 100 µl/min:

$$Re = U D_h \frac{\rho}{\mu} \qquad (3)$$

$$= 55.6\ 10^{-3} * 58\ 10^{-6} * \frac{10^3}{10^{-3}} = \underline{3.23}$$

- The ratio between the channel length and the hydraulic diameter is:

$$\frac{L}{D_h} = \frac{20}{58} = 0.34$$

which is less than 0.5.(see Table 3)

The restriction model yields a pressure difference proportional to the flow of the fluid. We have from equation (1):

$$\Delta P = \frac{C\,\mu}{2A\,D_h} Q \qquad (4)$$

$$\Delta P_1 = \frac{96 * 10^{-3}}{2 * 30\ 10^{-9} * 58\ 10^{-6}} * 16.7\ 10^{-12} = \underline{0.46}\ \frac{N}{m^2}\ \text{per}\ \frac{\mu l}{min}$$

With the flow both in the end and in the side channels the pressure difference can be expressed in an equivalent to Ohms law: the pressure difference is equivalent to the voltage, the flow to the current and the two flow channels to a parallel connection of two resistors:

$$\Delta P_{1+2} = \frac{R_{End}\,R_{Side}}{R_{End} + R_{Side}} Q \qquad (5)$$

$$= \frac{27.6\ 10^9 * 40\ 10^9}{27.6\ 10^9 + 40\ 10^9} * 16.7\ 10^{-12} = \underline{0.273}\ \frac{N}{m^2}\ \text{per}\ \frac{\mu l}{min}$$

Second model: skin-friction drag.

The second approximation is based on the pressure drop from a flow between two infinite parallel plates.

The approximations for the second model are the same as for the first model: a fully developed laminar flow of an incompressible fluid. The flow is further assumed to have no flux in the z-direction.

- The flow in the channel is dominated by viscous forces because the flow has a fully developed flow profile, i.e. the channel length L is longer than the entrance length L_O needed to produce a fully developed flow profile at a flow rate of 100 µl/min.

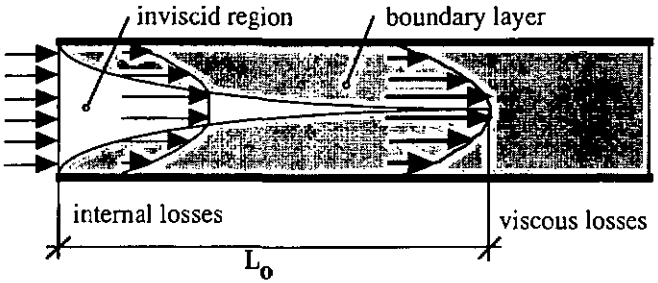

Figure 29 The development of a parabolic flow profile in a channel from a uniform entrance velocity.

$$L_O = 0.03\, D_h\, Re \qquad (6)$$
$$= 0.03 * 58\ 10^{-6} * 3.23 = \underline{5.74}\ \mu m$$

Which is smaller than the channel length of 20 µm.

In the infinite plate model there are only pressure alterations in the x-direction and only shear stresses acting in the y-direction.

The skin-friction model, equation (2), yields a pressure difference proportional to the flow of the fluid

$$\Delta P = 12\mu \frac{h}{a^3\, b}\, Q \qquad (7)$$

The pressure difference from the flow in the end channel will then be

$$\Delta P_1 = \frac{12 * 10^{-3} * 20\ 10^{-6}}{(30\ 10^{-6})^3 * 10^{-3}} * 16.7\ 10^{-12} = \underline{0.148}\ \frac{N}{m^2}\ \text{per}\ \frac{\mu l}{min}$$

or in both the end and the side channels with a calculation equivalent to that of (5)

$$\Delta P_{1+2} = \frac{8.89\ 10^9 * 40\ 10^9}{8.89\ 10^9 + 40\ 10^9} * 16.7\ 10^{-12} = \underline{0.121}\ \frac{N}{m^2}\ \text{per}\ \frac{\mu l}{min}$$

Comparing the two models given in equations (4) and (7), shows that the second approximation has the channel length as a factor and the cubic root of the width of the channel.

$$\frac{C\ \mu}{4}\ \frac{a+b}{a^2\ b^2} \sim 12\mu\ \frac{h}{a^3\ b}$$

For a « b this gives

$$\frac{2}{a^2\ b} \sim \frac{h}{a^3\ b} \qquad (8)$$

thus for h = 2 * a the two models yields the same result. This, coincidentally, is the case for the side channels.

Since the cantilever is pre-stressed against the flow direction by 20 μm due to the fabrication, the end channel is comparable to two infinite plates only for flow rates between 50 and 100 μl/min. The first approximation must therefore be expected to yield the best result for low flows.

In the laminar flow region, both models predict a linear relation between the flow and the pressure difference over the cantilever.

Electrical output from the pressure difference.

The pressure difference acting on the cantilever creates a moment in the thinner suspension of the cantilever. The surface stress from this moment is detected by four piezo resistors connected in a Wheatstone bridge [28].

- The moment in the thinner suspension is independent on whether the pressure difference is considered a line load on a flexible beam or a central force acting on a rigid beam.

$$M = \Delta P \, A_{Cant} \, \frac{l_2}{2} \tag{9}$$

With the result from (5) in the first approximation (9) yields

$$M = 0.27 * 3\ 10^{-6} * \frac{3\ 10^{-3}}{2} = \underline{1.23}\ 10^{-9}\ \text{Nm per}\ \frac{\mu l}{\text{min}}$$

- The surface stress in the thinner suspension is constant.

$$\sigma = \frac{\frac{h}{2} M}{I}$$

where $I = \frac{(2 w_1)\, h^3}{12}$

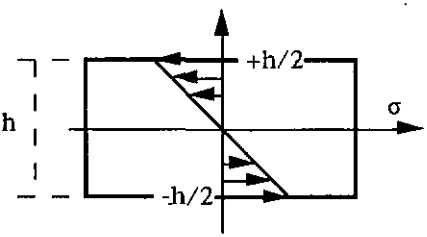

Figure 30 Stress distribution in a bent beam

$$\Delta\sigma = \frac{3}{2} \frac{l_2^2\, w_0}{w_1\, h^2} \Delta P \tag{10}$$

With the result of (5) this yields

$$= \frac{3}{2} \frac{(3\ 10^{-3})^2 * 10^{-3}}{400 * 10^{-6} * (20\ 10^{-6})^2} * 0.273 = \underline{23\ 10^3}\ \text{Pa per}\ \frac{\mu l}{min}$$

The sensitivity of the piezo resistors in the Wheatstone bridge is given by the factor K_G.

$$\frac{\Delta U}{U} = \frac{\Delta R}{R} = K_G\, \Delta\sigma \qquad (11)$$

This factor will be found and the sensitivity calculated

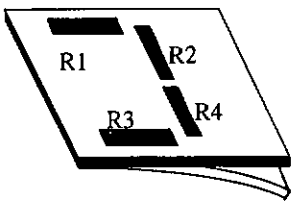

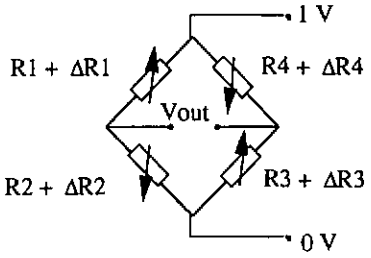

Figure 31 Four piezo resistors on the cantilever suspension

Two resistors (1&3) are placed parallel and two (2&4) transversal to the stress and the 110 cristaline direction of the silicium.

- The factor is given as
  (π_{ij} are the piezo resistive coefficients)

$$\frac{\Delta R}{R} = \pi_l\, \sigma_l + \pi_t\, \sigma_t \qquad (12)$$

$$\pi_l = \frac{\pi_{11} + \pi_{12} + \pi_{44}}{2}$$

$$= \frac{6.6\ 10^{-11} + -1.1\ 10^{-11} + 138.1\ 10^{-11}}{2} = \underline{71.8\ 10^{-11}}\ \text{Pa}^{-1}$$

$$\pi_t = \frac{\pi_{11} + \pi_{12} - \pi_{44}}{2}$$

$$= \frac{6.6\ 10^{-11} + -1.1\ 10^{-11} - 138.1\ 10^{-11}}{2} = \underline{-66.3\ 10}^{-11}\ Pa^{-1}$$

The two piezo resistor R_1 and R_3 are placed parallel to the deflection stress, thus

$$\frac{\Delta R/R}{\sigma_l} = \pi_l \qquad (13)$$

$$= \underline{71.8\ 10}^{-11}\ Pa^{-1}$$

The two piezo resistor R_2 and R_4 are placed perpendicular to the deflection stress, thus

$$\frac{\Delta R/R}{\sigma_l} = \pi_t \qquad (14)$$

$$= \underline{-66.3\ 10}^{-11}\ Pa^{-1}$$

With the relative output of the Wheatstone bridge is given by

$$\frac{V_{out}}{V} = \frac{1}{4}\left(\frac{\Delta R1}{R1} - \frac{\Delta R2}{R2} + \frac{\Delta R3}{R3} - \frac{\Delta R4}{R4}\right) \qquad (15)$$

the factor can then be calculated to

$$K_G = \underline{69.05\ 10}^{-11}\ [Pa^{-1}]$$

- The theoretical sensitivity of the sensor can then be found from (11) and the result of (5) in the first approximation.

$$\frac{\Delta U}{U}|_{FLOW} = \underline{18.8}\ \mu V/V\ \text{per}\ \frac{\mu l}{min} \qquad (16)$$

There are some factors not considered in equation (16)

- The leakage current,(about 0.2 μA), in the pn-junction is assumed unimportant due to the relatively large currents in the bridge (about 70 μA).
- Series resistors formed by the diffused conductor lines are not considered due to the very high difference in doping level.
- Self heating of the resistors and temperature dependence of the doped resistors are not taken into account because of the high heat conductivity of silicon (and of water) and because of the Wheatstone bridge connection out balances an even drift of all resistors, as seen from equation (15).

Deflection of the cantilever

The cantilever is pre-stressed to the piezo resistor side, against the flow direction. This is due to the thermal expansion coefficient of the silicon nitride layer, used to insulate the piezo-resistors, being higher than the coefficient for silicon and silicon dioxide. The deposition at 1100 °C gives a tensile stress on the cantilever surface which is measured as being about 25 µm at the end of the cantilever. As the thicker part of the beam (length l_2) hardly bends, The force F on the end of the beam produces a moment M at the end of the suspension (length l_1) which shows up as compressive and tensile stress in the silicon. If d_1 is the deflection at the end of the suspension, at that point the beam has an angle ß, and d_2 is the deflection due to the angle of the thicker part of the beam, $d_{tot} = d_1 + d_2$ is the total deflection.

We have:

$$d_2 = l_2 \sin ß \approx l_2 ß \tag{17}$$

$$ß = - \frac{M l_1}{2E I} \tag{18}$$

$$d_1 = \frac{M l_1^2}{2 E I} \tag{19}$$

$$I = \frac{2 w_1 h^3}{12} \tag{20}$$

$$M = F l_2 \tag{21}$$

and combining (17) to (21):

$$d_{tot} = \frac{2 l_2^2 l_1 + l_2 l_1^2}{E I} F \tag{22}$$

Combining (9), (10) and (11) a force sensitivity for a force applied at the free cantilever end can be determined

$$\frac{\Delta U}{U}\Big|_{FORCE} = K_G \frac{3 l_2}{w_1 h^2} \qquad (23)$$

$$= 69.05\ 10^{-11} \frac{3 * 3\ 10^{-3}}{0.4\ 10^{-3}\ (20\ 10^{-6})^2} = \underline{46.1}\ \frac{\mu V}{V} \text{ per } \mu N$$

Combining (22) and (23) yields a displacement sensitivity of

$$\frac{\Delta U}{U}\Big|_{DISP} = K_G \frac{E\ h}{4\ l_1\ l_2 + 2\ l_1^2} \qquad (24)$$

$$= 69.05\ 10^{-11} \frac{169\ 10^9\ 20\ 10^{-6}}{3.6\ 10^{-6} + 0.18\ 10^{-6}} = \underline{733}\ \frac{\mu V}{V} \text{ per } \mu m$$

Discussion

All the given sensitivities are dependent on the beam thickness and on the border between the thinner and the thicker part of the suspension. The beam thickness will in a successful etch vary ± 10 %, that is between 18 µm and 22 µm .As seen from figure 25, the length of the thinner part can be extended by roughly 0.4 mm, taking into account the etch profile. The total length $l_1 + l_2$ will however not be affected.

$h = [18; 22]$ µm $l_1 = 700$ rather than 300 µm
$l_2 = 2600$ rather than 3000 µm

Table 5 resumes the results and lists the minimum and the maximum limits given by the alterations

Table 5 Formula overview

Parameter	unit	mean	h_{min}	h_{max}	
$\frac{\Delta U}{U}\vert_{FLOW,1stAPP.}$	µV/V per $\frac{\mu l}{min}$	14.1	17.4	11.7	(10),(11)
$\frac{\Delta U}{U}\vert_{FLOW,2ndAPP.}$	µV/V per $\frac{\mu l}{min}$	6.4	7.0	5.7	(7),(10)
$\frac{\Delta U}{U}\vert_{FORCE}$	$\frac{\mu V}{V}$ per µN	40.0	49.4	33.0	(23)
$\frac{\Delta U}{U}\vert_{DISP.}$	$\frac{\mu V}{V}$ per µm	334	301	369	(24)
$\frac{F}{Q}\vert_{FLOW,1stAPP.}$	µN per $\frac{\mu l}{min}$	0.35	0.35	0.35	(5),(9)
$\frac{F}{Q}\vert_{FLOW,2ndAPP.}$	µN per $\frac{\mu l}{min}$	0.16	0.14	0.17	(7),(9)

3.4 Characteristics

Flow sensitivity measurements

All sensitivity measurements, flow, force and displacement, have been done on the same sensor so as to obtain correlation between the results.

Experimental set-up

The experimental set-up for the flow sensitivity measurements gave an electrical output as a function of a flow in the 15 µl/min to 200 µl/min range.

For the sensitivity measurements the flow sensor was glued on a PCB print and protected by two plastic tubes, as shown in figure 32. This allowed a free bending of the cantilever, with its deflection limited in the flow direction at the PCB.

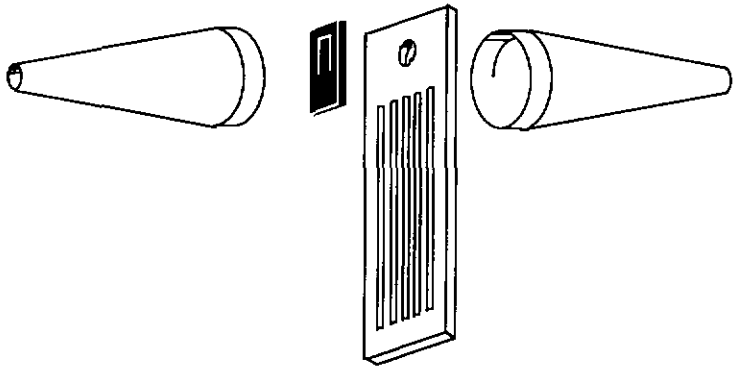

Figure 32 The sensor mounting for the flow sensitivity measurements.

The mounted flow sensor was connected in the arrangement shown on figure 33. The flow was from right to left, and was controlled by adjusting the height of the source vessel or by blocking the tubing with a clamp. A Mettler AE240 balance, interfaced to a computer measured the flow. In the test arrangement the flow sensor was covered, as the PN-junction between the implanted conductors and the substrate is sensitive to light.

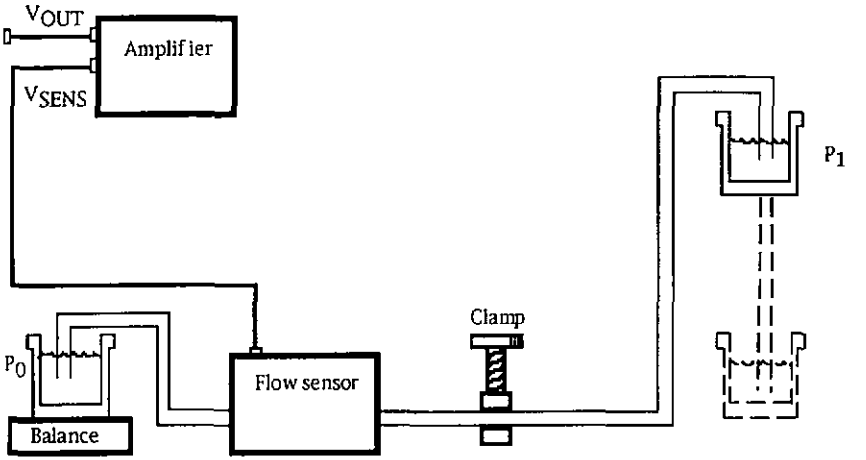

Figure 33 The experimental set-up for the flow measurement.

Results

The experimental results show a clear linear dependence. No difference in sensitivity was observed due to the different absolute pressure over the sensor with the vessel or the clamp regulation.

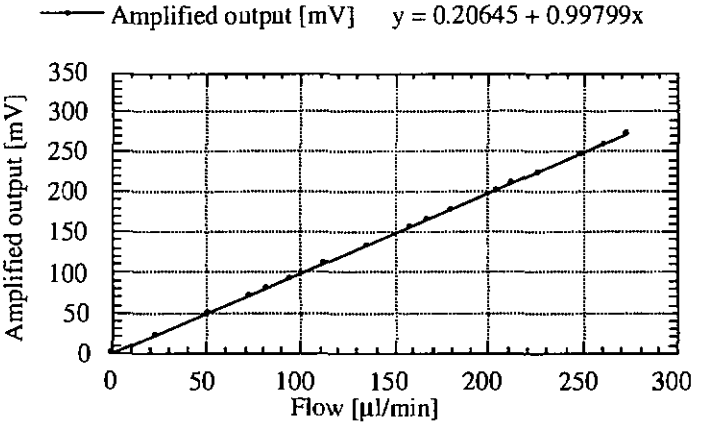

Figure 34 Sensor output plotted versus the flow of de ionised water. Sensor output is amplified 100 times.

The unamplified **measured flow sensitivity** of the sensor is

$$10\ \mu V \text{ per } \frac{\mu l}{min}$$

measured with a voltage drop of 1 V over the Wheatstone bridge.

The **theoretical flow sensitivity** is

11.7 to 17.4 $\frac{\mu V}{V}$ per $\frac{\mu l}{min}$ for the restrictive drag model.

5.7 to 7.0 $\frac{\mu V}{V}$ per $\frac{\mu l}{min}$ for the skin friction drag model

The flow sensitivity of the sensor is comparable to the calculations using the first model.

Force sensitivity measurements.

Experimental set-up.

The experimental set-up for the force sensitivity measurements gave an electrical output as a function of an applied force in the 20 μN to 1800 μN range.

The connected flow sensor, before mounting the fluid interface, was placed on a stable support and the point of a wire spring was placed near the end of the cantilever. The fixed end of the wire spring was then displaced vertically. The relation between the displacement and the force of the spring point was found by pushing on a Mettler AE240 electronic balance with the spring point as shown in figure 35.

The force was applied at the end of the cantilever because it was easier to place the point precisely at the end of the cantilever than precisely in the middle.

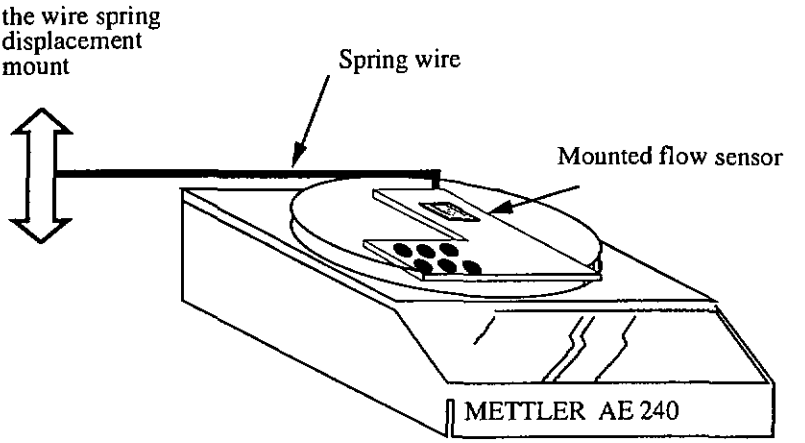

Figure 35 Measurement set-up

Results.

The experimental results shows a clear linear dependence.

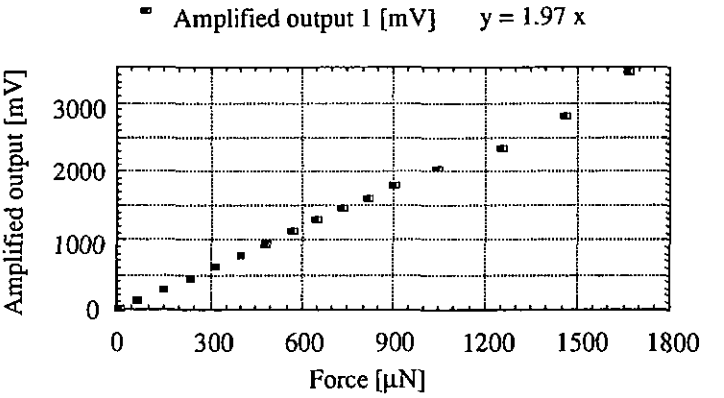

Figure 36 The sensor output plotted versus applied force.
The sensor output is amplified 100 times.

The unamplified **measured force sensitivity** of the sensor is

$$20 \qquad \frac{\mu V}{\mu N}$$

measured with a voltage drop of 1 V over the Wheatstone bridge.

When combined with the last two expressions of table 5, we have for the first model:

$$7 \qquad \mu V \text{ per } \frac{\mu l}{min}$$

and for the second model:

$$\text{from} \quad 2.8 \text{ to } 3.4 \qquad \mu V \text{ per } \frac{\mu l}{min}$$

This is to be compared with the result of the flow sensitivity which was:

$$10 \qquad \mu V \text{ per } \frac{\mu l}{min}$$

These last results are a slightly lower than the flow sensitivity values. The force was applied as close to the edge as possible, but not on the edge. This misplacement will yield a somewhat lower output for a given force as seen from (23).

Displacement sensitivity measurements

Experimental set-up

The experimental set-up for the displacement sensitivity measurements gave an electrical output as a function of a displacement in the 0 μm to 50 μm range.

The mounted sensor was placed under a UBM optical scanner and displaced with a wire spring as shown in figure 37. After each displacement of the fixed end of the wire spring, the UBM scanned a trace over the edge of the free end of the cantilever over on the sensor surface. From this trace the relative distance between the free cantilever end and the sensor surface was measured.

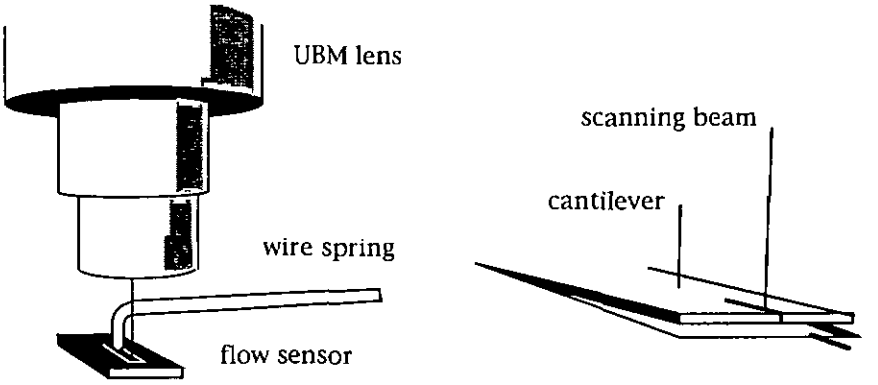

Figure 37 Experimental set-up for displacement measurements

Results

The experimental results shows a clear linear dependence for the sensor.

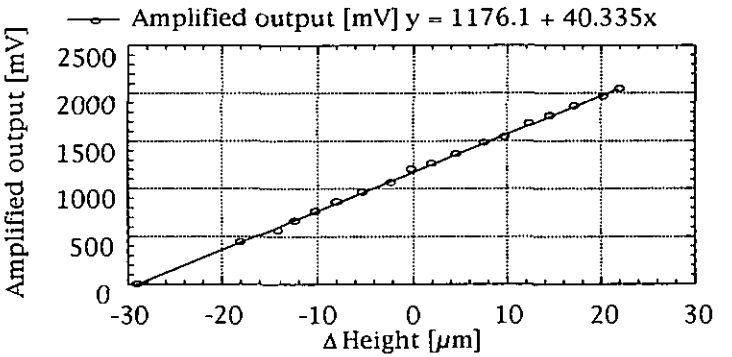

Figure 38 Sensor output plotted versus displacement.
The sensor output is amplified 100 times.

The unamplified **measured displacement sensitivity** of the sensor is

$$400 \quad \frac{\mu V}{\mu m}$$

measured with a voltage drop of 1 V over the Wheatstone bridge.

This is to be compared with the theoretical displacement sensitivity as seen from table 5.

$$301 \text{ to } 369 \quad \frac{\mu V}{\mu m}$$

The results show good correlation between theory and practical measurement.

Flow profile simulation

Using numerical flow-profile simulation, the flow through the sensor has been determined and the resulting pressure distribution on the cantilever beam calculated. This was done in order toverify the flow models (This work was subcontracted to Sulzer Innotec, Winterthur, Switzerland)

Using the simulation program TASKflow, the geometrical boundaries of the flow sensor, represented by 81'000 mesh knots, were entered into a computer. As boundary conditions, a volumetric flow of 50 microliters per minutes of water at ambient temperature was considered to be established.

The results show that the relative velocity of the fluid increases by a factor 100 inside the opening and due to the rapid expansion of the flow channel after the slit, a low velocity back-flow of the water appears. This is shown in figures 39 and 40. These figures show half of the sensor's front opening, x-z plane, as viewed along the y-axis.(see table 2)

The static pressure drop calculated is 4.05 N/m^2 at 50 microliters per minute which corresponds to a force exerted on the beam of 0.24 µN per µl/min. This result is in the same order of magnitude as the values of table 5.

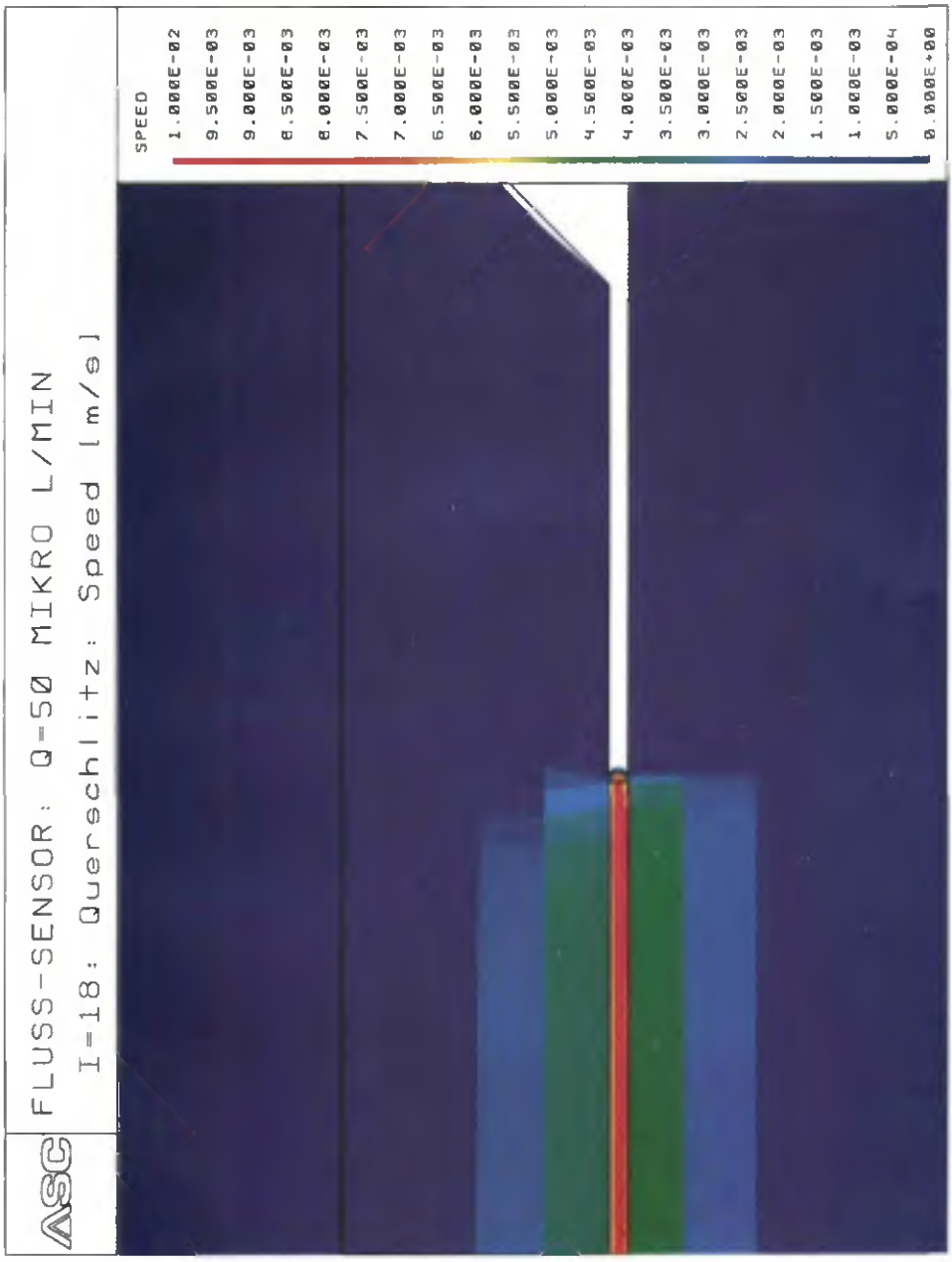

Figure 39 Speed of water through sensor.

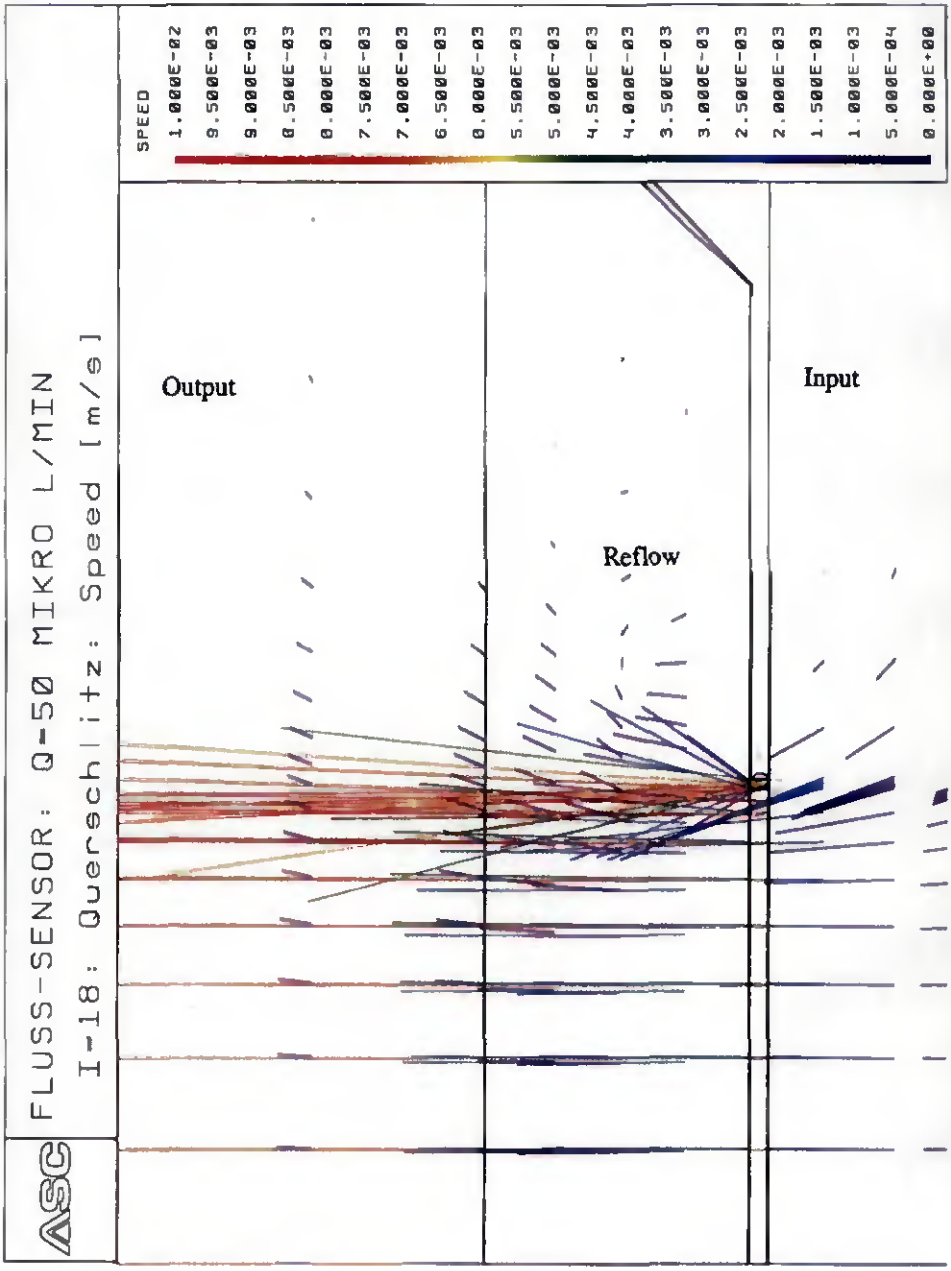

Figure 39 Water speed vectors through sensor.

3.5 **Conclusion**

As seen in the previous results, both analytical models used show a good correlation. The results from the orifice model are closer to the practical measures. This has been verified making measures with variable geometries [29].

However the measurement methods for force and displacement are relatively rugged compared to the precision required. The fact that the sensor's force and displacement characteristics are measured prior to encapsulation must also be taken into account as this process step can induce strains into the sensor and alter the results.

4. Regulated Micropump

After having described the the micro pump and the flow sensor, the present chapter deals with the integration of these two components into a regulated device. The regulation will first be approached analytically and the practical results will be shown.

4.1 Introduction

As presented in chapter 2, the micro pump's output is influenced by a certain number of disturbances. These can be classified into internal and external disturbances. The external disturbances are pressure variations at input or output or changes in the channel geometry outside the pump. The internal disturbances are due to bubbles in the pump, bad sealing of the valve seats or ageing of the piezo disc.

The main problem, which will be discussed in the present chapter, is the differential pressure dependence as shown in figure 18 [30,31].

So as to compensate the effect of pressure variations, the pump will be operated as a feedback control system. For a system to be classified as a feedback control system, it is necessary that the controlled variable, in the present case the flow rate, be fed back and compared with the reference input. In addition, the resulting error signal must actuate the control elements to change the output so as to minimise the error. A feedback control system is also called a closed-loop system.

In contrast to the closed-loop system, in the open-loop system there is no comparison of the controlled variable with the desired input. Each setting of the input determines a fixed operating position for the control elements. Thus for a given set input, there may be large variations to the controlled variable due to the disturbances [32].

A major advantage of employing feed-back control is that, because of the comparator, the actuating signal continually changes so that the controlled variable tends to become equal to the reference input regardless of the disturbances. Another consideration is that with feedback one can generally use relatively inexpensive components and yet achieve better control than is possible with very expensive components in an open-loop system.

4.2 Analytical approach

In order to simplify the analytical regulation, all physical variables are expressed in the same unit. Hence the pump is coupled to the flow sensor and both input and output are expressed in volts. The actual flow rate does not need to be taken into account as the pump "transforms" the actuation voltage into flow which in turn the sensor "transforms" back into a voltage. (see figure 41) The effects of the flow channels linking the discreet components to each other and to the outside world are integrated in the components characteristics.

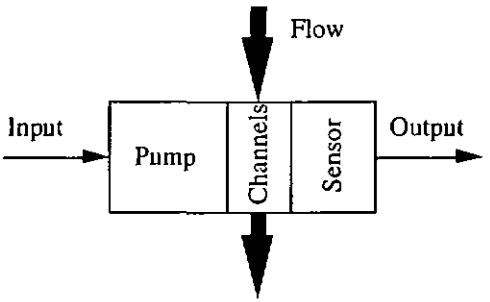

Figure 41 Open-loop pump system.

The function relating the input to the output is called the transfer function. For an open-loop system we have:

$$(\text{input}) \times \mathbf{K} = \text{output} \tag{25}$$

The transfer function is the ratio of two variables expressed in the same units, hence it is unitless.

In a closed-loop system the output is compared with a desired reference or set-point if it is constant. The difference between reference and output is called the error which yields the feedback signal once fed through the controller. the feedback then acts on the input so as to minimise the error. (see figure 42)

The relation between error and feedback is the transfer function of the controller. We have:

$$(\text{error}) \times \mathbf{G} = \text{feedback} \tag{26}$$

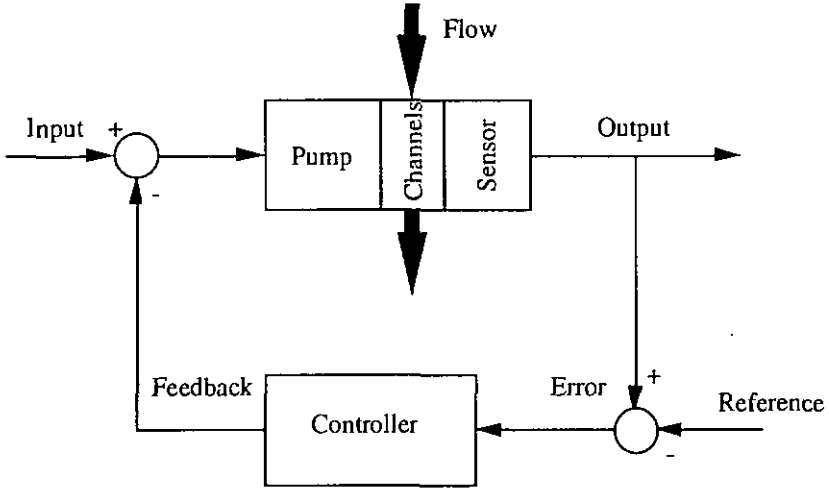

Figure 42 Closed-loop pump system.

The combination of the open-loop and feedback transfer functions characterise the complete system. The next step is to determine the transfer function of the open-loop system, chose a certain type of controller and implement its transfer function.

The most powerful methods of system analysis have been developed for linear control systems. For a linear control system all the relationships between the variables are linear differential equations, usually with constant coefficients. The reason that differential equations rather than algebraic equations are obtained is that in feedback control systems the variables are functions of time. Actuator control systems usually contain some non-linear elements. Such elements would in turn yield non-linear differential equations for the system. For many components encountered in control systems, the operating characteristics are given in form of general operating curves rather than equations. These curves can be analysed and a linear approximation fitted around the point of reference or the range of operation if possible.

All systems have two main modes of operation: the steady-state operation and the transient condition. By steady-state operation is meant the equilibrium state attained such that there is no change with respect to time of any of the systems variables. The system remains at this equilibrium state of operation until it is exited by a change in the desired input or in the external disturbances. A transient condition is said to exist as long as any of the variables of the system is changing with time.

We will assume that the components are described by linear differential equations with constant coefficients. For a known input, constant or varying in time, classical methods can be used to determine the output. However, considerable time is saved by using the Laplace transform method of solving linear differential equations. In addition, Laplace transform analysis are closely related to other methods for evaluating system performance. The Laplace transformation of a function of time f(t) is noted F(s).

$$F(s) = \mathbf{L}[f(t)] = \int_0^\infty f(t)\, e^{-st}\, dt \qquad (27)$$

where $\mathbf{L}$ is the symbol for taking the Laplace transform. For the integral on the right side of cquation (27) the variable t vanishes after evaluation between the limits of integration. Thus the resulting expression is a function of s only.

Open-loop transfer function

The open-loop transfer function in the time domain k(t) is a constant. If x(t) is the input and y(t) the output we have:

$$k(t) = \frac{y(t)}{x(t)} \qquad (28)$$

The pump and sensor must be considered as one element. If $\varphi(t)$ is the flow rate as a function of time and $V_p(t)$ the voltage at the entrance of the high-voltage cascade producing the excitation of the piezo, we have the pump characteristic:

$$\varphi(t) = a_1\, V_p(t) + a_2$$

For the flow-sensor, $V_s(t)$ being the output voltage, we have:

$$\varphi(t) = b_1\, V_s(t) + b_2$$

The combination of these two equations yields:

$$V_s(t) = \frac{a_1}{b_1} V_p(t) + \frac{a_2 - b_2}{b_1} \qquad (29)$$

To determine the transfer function k(t) would be relatively difficult as the effects of the pump, the sensor, the flow channels and the electronics have to be taken into account. The steady-state operating conditions are well known, see figure 17, but the transient state is defined from the practical results. It is simpler to determine the Laplace transform K(s). This can be done practically by first determining the order of the system. If the response to a unit step voltage does not "overshoot" the desired value, the system is said to be a first order system.

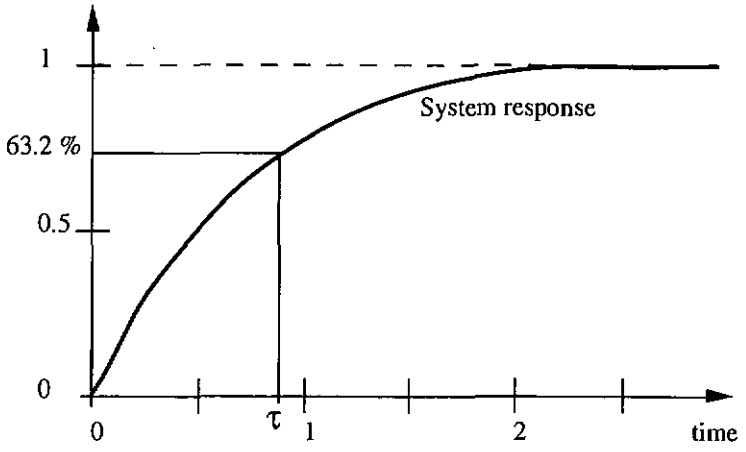

Figure 43 Response to unit step of a first order system

The transfer function can be written as follows:

$$K(s) = \frac{A_o}{1 + \tau\, s} \qquad (30)$$

Where A_o is the static gain of the system and τ the open-loop time constant of the system defined as being the time the system takes to reach 63.2 % of its final value. (the vertical axis on figure 43 is normalised)

Controller transfer function

Depending on the system we want to regulate and the type of regulation, the controller will be chosen.

The simplest system is the proportional control system. In this case the error is amplified by a factor P_o, called the gain of the regulator, and this amplified error is then subtracted from the input. The proportional control system establishes a linear relationship between the error and the feedback. In a lot of cases this type of regulation is sufficient, that is if the perturbation is transient, its effects on the system will be diminished.

If an external load is applied to the system, for example change in diameter of the tubing thus variation in the flow resistance, the reference will not quite be respected. As a matter of fact, an increase in channel resistance causes a drop in flow rate. The error signal becomes negative, and the feedback increases the input. The flow rate increases again but as the output approaches the reference, the error decreases (in absolute value) and the input value is again lowered before the reference is reached. The steady state operation of the system, if the output y and the reference r are different, will be:

$$y = \frac{K - K P_o r}{1 + K P_o} \tag{31}$$

This steady state error is called the static error. To compensate this phenomena and maintain a reference output under long perturbations, the history of the error signal must be taken into account. This is obtained by integrating the error signal and adding this integral to the error signal itself before multiplying it with the gain P_o. The feedback signal can be expressed by the following expression:

$$f = P_o \left[r + \frac{1}{Ti} \int_0^t r \, dt \right] \tag{32}$$

In equation (32) T_i is the time constant of the integrator. We now look at what happens when the output changes due to a constant load. The error signal absolute value increases, the feedback signal increases and if the response time of the open-loop system is slower than that of the controller, the output will increase until it reaches the reference value. At that point the error is zero and the feedback signal stays constant.

We can see that if the regulator reacts too fast, the reference value will be passed and the system will oscillate around the reference value. This means that the choice of the regulation constants P_o and T_i determines the stability of the regulated system.

It is possible to add a differential loop in the regulator, making a well known PID-regulator. In this case the differential contribution would yields a larger regulation signal on fast disturbances. These are automatically damped in the present configuration due to the elasticity of the fluid connections.

An advantage of having chosen a standard type of regulation, the proportional-integrating or PI-regulation, is that the transfer function are well known. For a PI-regulator, the control loop ,can be expressed by the following expression in the s domain:

$$G(s) = P_o\left[\ 1\ +\ \frac{1}{s\ T_i}\right] =\ P_o\frac{1\ +\ s\ T_i}{s\ T_i} \qquad (33)$$

System transfer function

The transfer function of the system can now be calculated. We have:

$$H(s) = \frac{K(s)}{1\ +\ K(s)\ G(s)}$$

when replacing the values from equations (30) and (33) we have:

$$H(s) = A_oP_o\ \frac{1\ +\ s\ T_i}{s^2(\tau T_i) + s(T_i\ +\ A_oP_oT_i) + A_oP_o} \qquad (34)$$

This function has two poles. The poles of this equation are the values of s for which the denominator is equal to zero. The value of the poles determine the stability of the system.

A closed-loop system is stable if the poles of the transfer function H(s) are complex and negative numbers.

4.3 Testing **and results**

The regulated system must be able to deliver a constant flow rate even if the pressure difference between input and output varies.

The pump will be actuated at 40 Hz and the characteristic linearized.

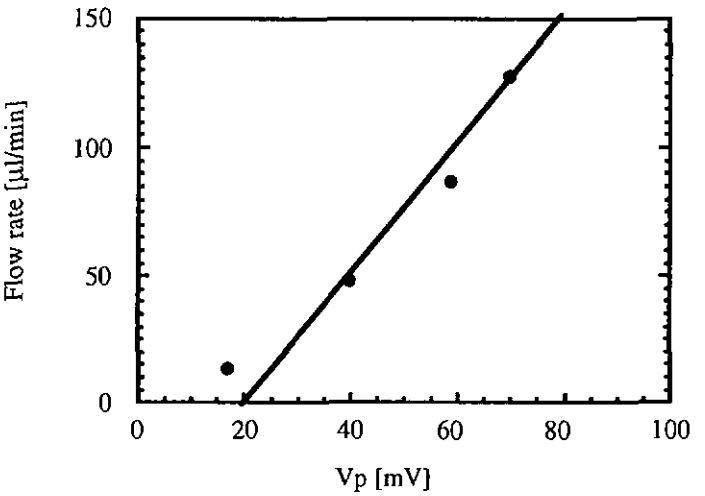

Figure 44 Pump flow rate characteristic at 40 Hz actuation frequency expressed as function of the input voltage

The amplification factor of the driver electronics is taken into account. This means that the approximation of the pump characteristic is (voltage in millivolts and flow rate in µl/min):

$$\varphi(t) = 2.5\ V_p(t) - 45$$

The output signal of the system is based on the sensor signal. The sensor signal has been amplified. Figure 45 shows the system output versus flow rate. We have (in this equation, voltage is expressed in millivolts and flow rate in µl/min):

$$\varphi(t) = 0.1\ V_s(t) - 30$$

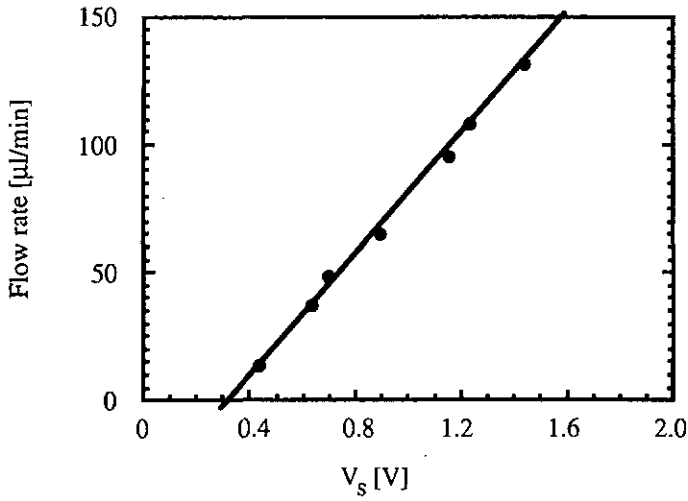

Figure 45 Sensor flow rate characteristic expressed as function of the system output voltage

When replacing the measured values in equation (29) we can obtain the steady state open loop relation between input and output:

$$V_S(t) = 25{,}9\ V_p(t) - 158 \qquad (35)$$

If we take as reference point 90 µl/min, it corresponds to a output voltage of 1.2 volts and an input voltage of 50 millivolts. Figure 46 shows the response of the open-loop system to a unit (50 mV) step input.

We can see that the time constant is 1.1 seconds and the static gain 23. Equation (30) can be written as follows:

$$K(s) = \frac{23}{1 + 1.1\ s} \qquad (36)$$

To now determine the coefficients of the regulator the method of Ziegler-Nichols can be applied [33]. It consists in analysing the system step response. The intersection between the tangent to the step response at its point of inflection and the abscissa is called L. The normalised slope of the tangent is called a. We have:

$$P_o = \frac{0.9}{a\ L} \qquad \text{and} \qquad T_i = 3.3\ L \quad [s] \qquad (37)$$

The point of inflexion is difficult to determine. From figure 46 we can determine L = 0.08 and a = 0.83. When replacing these values in equation (37) we have:

$$P_o = 13.5 \qquad \text{and} \qquad T_i = 0.26 \qquad [s] \qquad (38)$$

which yields from equation (33):

$$G(s) = 13.5 \frac{1 + (0.26)\, s}{(0.26)\, s} \qquad (39)$$

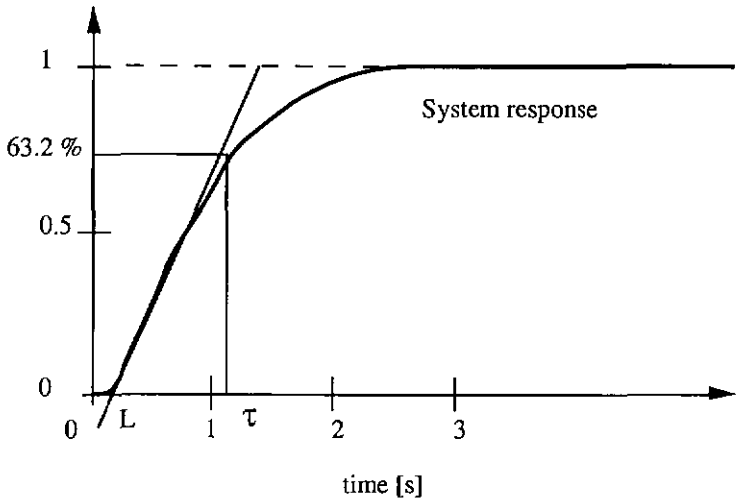

Figure 46 System response to unit step

From equations (34), (36) and (39) we can determine the transfer function of the complete system:

$$H(s) = 310.5 \frac{1 + s\,(0.26)}{s^2(0.29) + s(81) + 310.5} \qquad (40)$$

The poles of this equation are $p_1 = -3.9$ and $p_2 = -275.4$. From these values we can conclude that the regulated system is stable.

Practical verification and regulation

According to the parameters above, a practical measurement set-up was mounted. A step corresponding to 420 µl/min was applied to the entrance of the regulation system. This corresponds to the maximum allowable actuation voltage on the pump and corresponding flow with no differential pressure applied. The rise time necessary to reach 90% of the desired output was less than one second. with no overshoot or oscillations.

The object of the present study is to operate the pump in a mode where the reference is imposed and does not change over time. Figure 47 shows the measurement set-up. The height of the inlet reservoir may be varied so as to create a differential pressure between input and output. This would practically be the case of a patient lying in bed and lifting his arm where a drug is infused. The difference of pressure must not influence the reference flow rate desired.

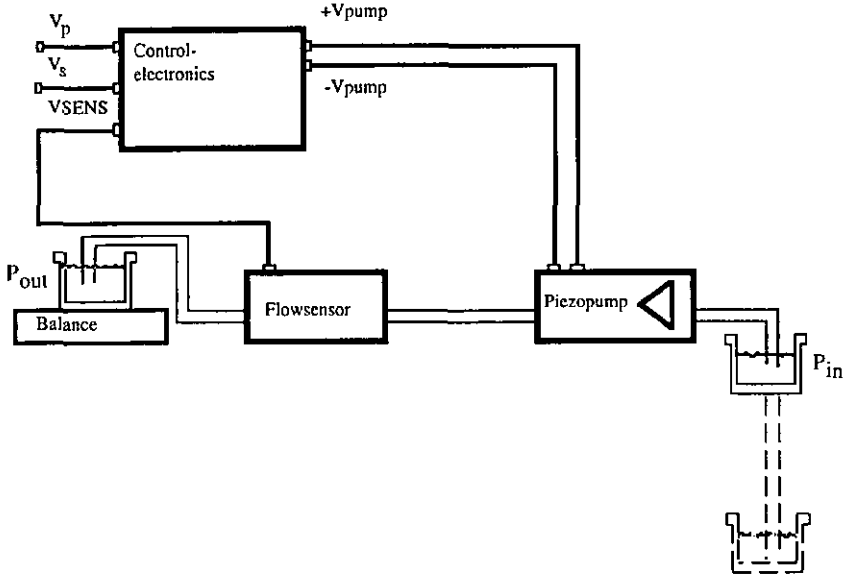

Figure 47 Measurement set-up

The flow rate is measured for different reference values, the reference being set at zero differential pressure. The inlet pressure is then lowered and the variations of the flow rate recorded.

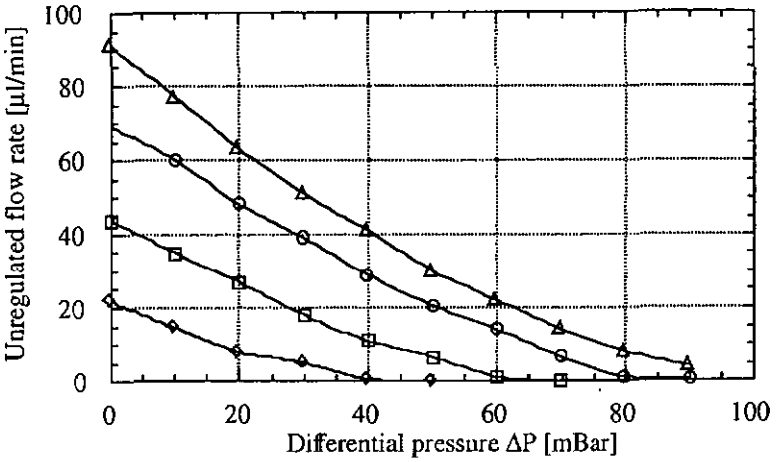

Figure 48 Unregulated flow-rate versus differential pressure

We can see that even small difference in pressure will change the flow rate significantly. This has been compensated successfully .

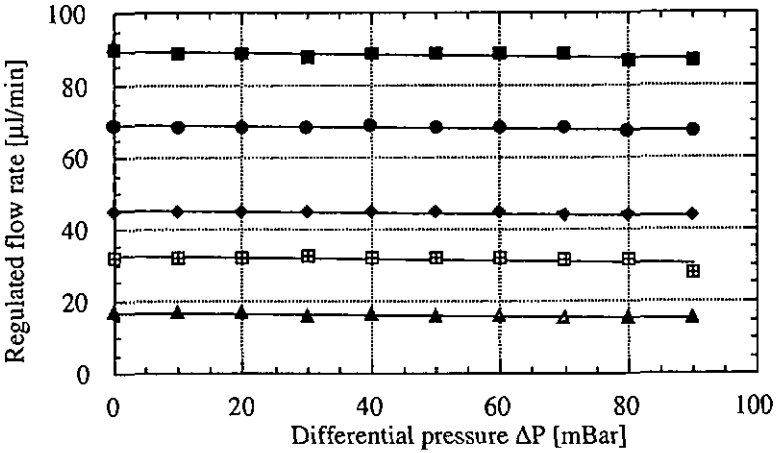

Figure 49 Regulated flow-rate versus differential pressure

The flow rate is maintained over the pressure range. Higher ranges can be achieved only within the limits of the pump capacity.

4.4 Conclusion

It has been demonstrated that the variations of the output flow rate of a micropump which are due to changes of the inlet pressure or the outlet pressure can be compensated by operating the pump in a feedback control system.

The stability of the controlled system is mainly due to the dampening induced by the elasticity of the interconnection tubing. As can be seen from figure 46, the system is of the first order. However the analysis of the system's behaviour has allowed an optimisation of the control parameters.

The implementation of the control loop has also the advantage of minimising the effects of internal disturbances, making the pump less sensitive to bubble formation and particle contamination. .

5. Micro-Torque sensor

This chapter describes a Micro-torque sensing system developed for the watch industry. This device allows absolute measurement of torque between 0 and 150 micro-newton-meter.

5.1 Introduction

Torque measurement is an essential item in the characterisation of Micro Electro-Mechanical Systems having rotating components. A high-resolution torque measurement device is presented. This device has been developed to answer a particular need in the characterisation of automatic watch mechanisms. Such torque measurement systems have recently been presented by Mikuriya et al., working in the range from 100 nN.m to 10 μN.m with a resolution of 10 nN.m. The size of the active part of this system is about 30 cm by 10 cm by 10 cm.[34] This system is used to characterise micromotors. A force meter is coupled to a meter shaft floated by air bearings to reduce friction. The torque acting on the shaft is proportional to the force applied to the force meter.

We propose a similar miniaturised approach using existing components such as the flow or force sensor presented previously [26]. This system combines classical high-precision mechanics and silicon technology.[35]

In the watch industry, a criterion of quality for mechanical self-winding wrist-watch mechanisms, is the amount of movement the user has to make per day to rewind the energy storage spring. This criterion depends mainly on the "dead angle" of the mechanism, that is the angle the oscillating mass has to cover until the spring is again wound up when the rotation of the mass changes direction. The lower the dead angle is, the higher the quality rating of the mechanism will be. The work required to move the oscillating mass depends on the efficiency of the mechanism. This efficiency can be determined by measuring the frictional losses between the oscillating mass and the energy storage spring.

To measure these frictional losses in order to classify the mechanisms in a serial production, a micro-torque sensor based on differential force measurement having a resolution of at least 0.5 μN.m over a range of -200 μN.m to 200 μN.m is required. At the end of 1992, this device was first tested in our institute giving satisfactory results.

5.2 Principle

The torque sensor is schematically represented in figure 50. It consists of two piezo resistive force sensors. A spring blade mounted perpendicular to the torque axis converts the torque to a force acting on the two force sensors. The force sensors are micro machined silicon cantilevers with piezo resistors doped in the bending suspension of the cantilevers [26].

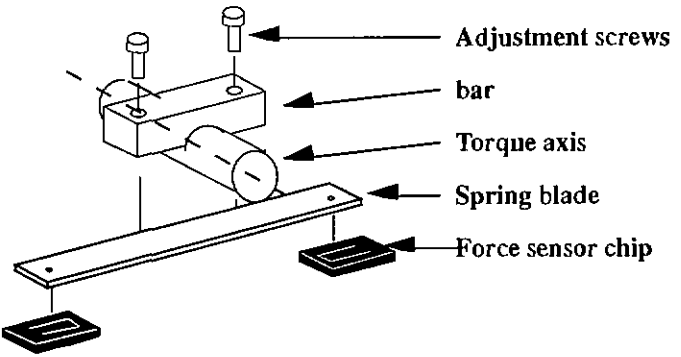

Figure 50 Schematical representation of micro-torque sensor

The piezo resistors are arranged in a Wheatstone bridge configuration and the voltage drop over the bridge is amplified.

A perpendicular bar is mounted on the torque axis. This bar acts on a spring blade by way of two adjustable screws. The spring blade acts through two points on two cantilever force sensors. The spring beam is pre-stressed by the pressure of the screws, and in the used range a torque applied on the axis will increase the pressure on one force sensor and decrease the pressure on the other.

The most fragile elements in the device are the silicon chips. To allow a safe use of the sensor, a mechanical end stop limits the rotation of the torque axis. This function is performed by a bolt passing through the torque axis into a hole. The difference of diameter between bolt and hole accounts for the rotational freedom of the torque axis.

Fabrication

The active element, a silicon chip shown in figure 51, is manufactured by standard planar technology coupled with bulk etching technologies. It is the same element as the flow-sensor chip presented earlier.

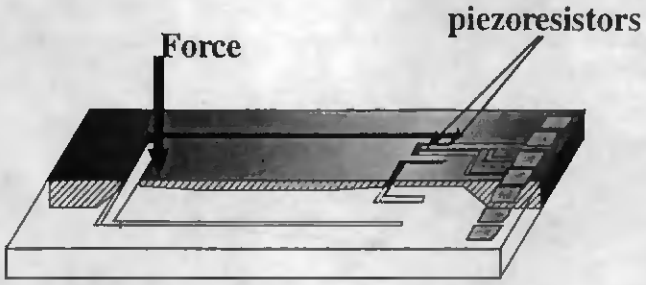

Figure 51 Force sensor chip.

The torque axis is mounted into two ruby bearings supported by a brass frame. The spring blade is a machined sheet of Copper Beryllium alloy having a thickness of about 100 µm. All parts are machined with a high precision to ensure optimal alignment of the bearings.

The configuration of the device allows to measure static torque only. To interface with the oscillating mass, a fork made of polyimide (perpendicular bar in figure 52) and silver-palladium spring wire having a diameter of 300 µm is mounted on the torque axis.

The chips are mounted on a printed circuit board with the control electronics. The electronic components are commercially available surface mounted devices. The complete printed circuit board is positioned precisely relatively to the brass frame. Mechanical precision is in the order of 10 µm. Bad positioning of the sensor chips will give different output values. To lessen the importance of the mechanical positioning, it is possible to adjust the offset and the gain of the control electronics.

5.3 Experimental results

The calibration of the torque sensor is achieved with the help of a Mettler AE240 balance by applying a known force on either of the sides of the perpendicular bar. (see figure 52)

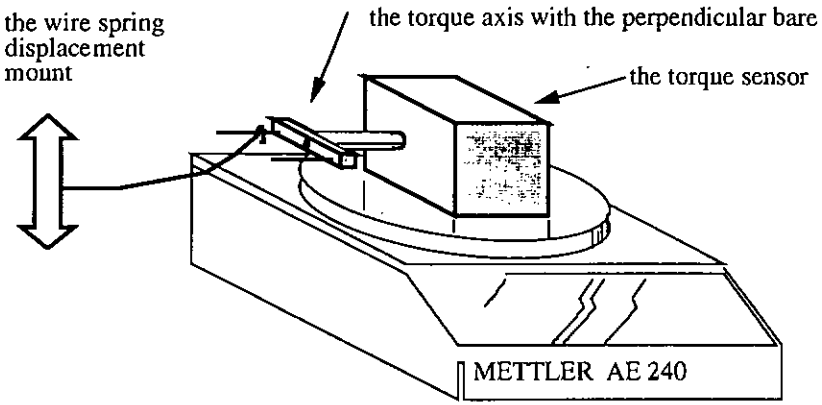

Figure 52 Calibration set-up

As expected from the force characteristic of the force sensor chip, and shown in figure 53, a linear characteristic is obtained with an amplified sensitivity of 4 mV per µN.m. Once mounted and adjusted, the device presents no measurable drift over time, about 6 months of use to this day, in a laboratory environment. This is in part due to the differential measurement principle. To increase the operating range of the device, the geometrical (reduction factor) environment has to be adapted.

The inner length between the two spring wires on the fork is 20 mm. The distance on the spring blade between the torque axis and the contact point is 14 mm. The ratio between these two distances yields the reduction factor. The point of application of the force is at 1 mm from the edge of the cantilever beam

A torque of 200 µN.m exerted on the torque axis corresponds to a force of 0.01 N on the sensor chip. This is an order of magnitude higher than the forces used to calibrate the sensor chip.(see figure 36)

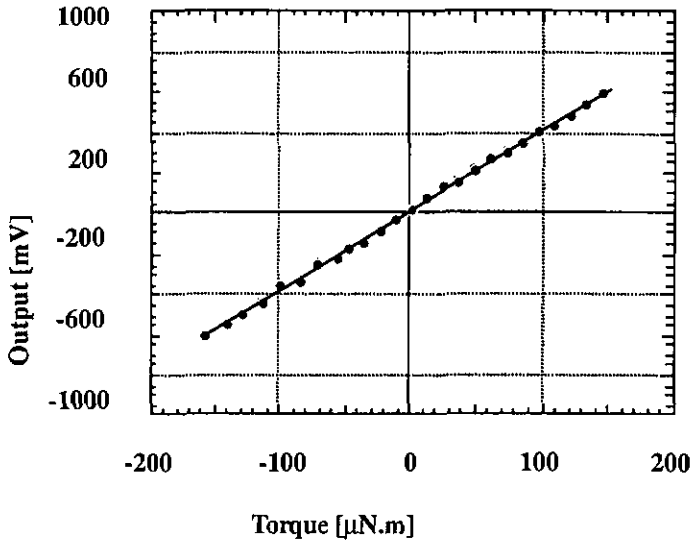

Figure 53 Sensor output vs. torque

We have seen that the sensitivity and range of the device depend on the geometrical set-up of the system. The limit of sensitivity of the force sensor chip has been demonstrated to be about 100 nN. If we consider a set-up where the half-length of the spring blade is 1 cm, the torque resolution for the device is 1 nN.m. We consider a practical sensitivity of 50 nN.m as the electrical noise from the circuit makes more precise measurements difficult. In the present case the range is limited by the mechanical end stop to +/- 200 µN.m.

The sensor (see figure 54) is mounted in a complex test bench that simulates the movement of the oscillating mass. The whole watch mechanism is rotated while a know torque, simulating the energy storage spring, is applied to one end of the gear train. On the other end of the gear train is the oscillating mass. The mass will be oriented downwards in the same position due to gravity when the system is at rest. As the mechanism rotates, the friction in the gear train as well as the torque simulating the storage spring will exert a torque on the oscillating mass. The sensing device is interfaced via the spring wires of the fork to the oscillating mass and the desired frictional torque can be acquired.

The primary motor rotates the mechanism as the torque motor acts on the gear train. An optical encoder monitors the angular displacement and speed.

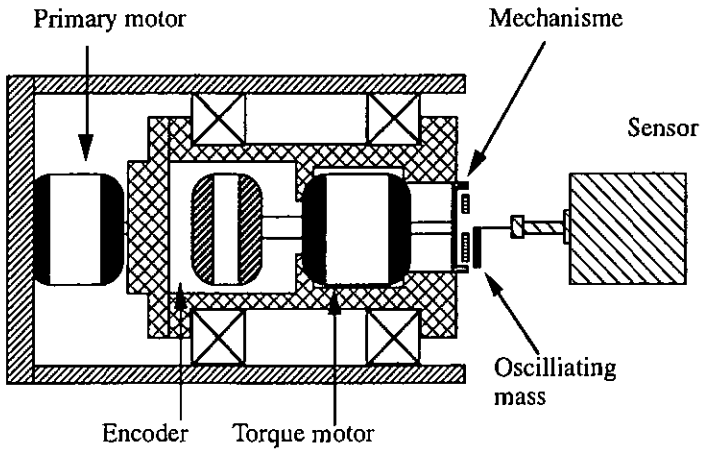

Figure 54 Wristwatch mechanism measurement set-up

Figure 55 shows experimental results on a wristwatch mechanism operated 6 turns clockwise and 6 turns counter clockwise at 10 rpm. The variations on the signal are due to the teeth of the gears inside the mechanism and particle contamination. With this result, the watch-makers can classify the mechanisms into high and low quality without human interference.

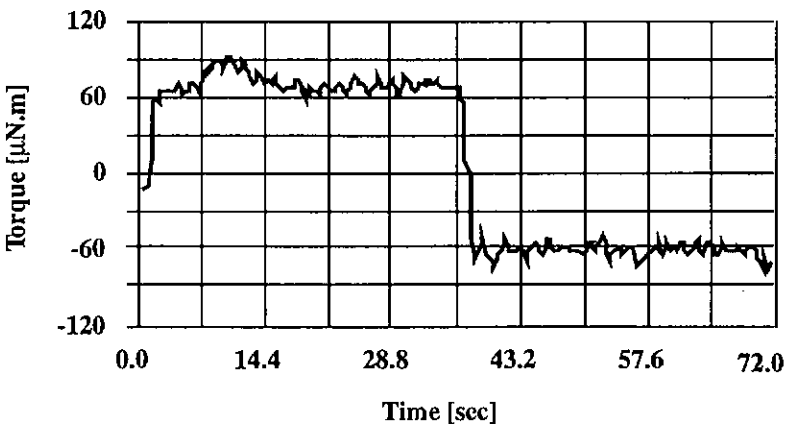

Figure 55 Friction torque on watch mechanism

Miniature motors are a field of intense research. The motor torque characteristics are often in the sub-micronewton meter range. The present device has been coupled to a hybrid integrated micromotor. [36]

The coupling was achieved on the basis of a friction clutch. The dynamic starting torque was measured to be 1.4 μN.m with this method, as shown in figure 56. The motor is coupled by friction to the torque sensor and then released.

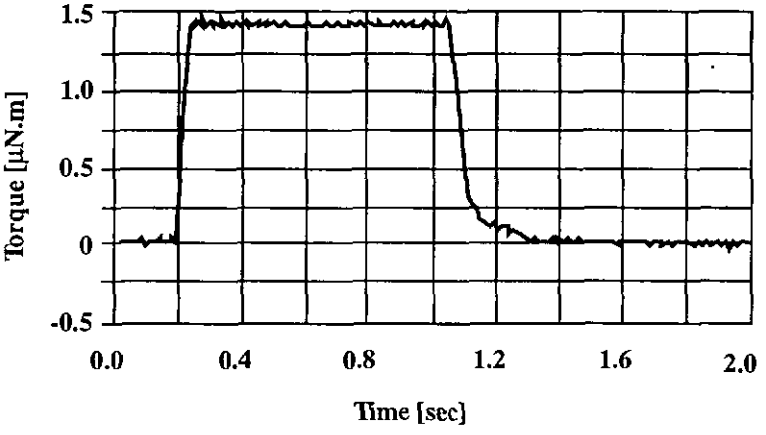

Figure 56 Dynamic torque of Hybrid Micromotor

When determined optically, the result obtained was 1.2 μN.m. This shows good correlation between the two measurement methods. The main advantage of the torque measurement device in this case is that the measurement is direct and rapid. It has the disadvantage of influencing the motor movement as some of the produced energy is absorbed in the coupling.

5.4 Conclusion

A novel miniaturised torque measurement system has been manufactured using the advantages of small size and good reproducibility given by micro-machined devices. This device is a good example of hybrid technology. It has allowed industrial production control in the watch-making industry and can be applied to numerous other problems.

6. Bone Implant Relative Displacement System

This chapter describes a hybrid system developed to measure the relative displacement of a hip bone implant. The system describes only uses readily available components to realise its function.

6.1 Introduction

Artificial hip joints are being implanted since numerous years. The quality of the implant and its "lifetime" vary from a few months in the worst case, to many years. The main problem is the stability of the socket placed inside the pelvic girdle. The aim of this type of implant fixation is to achieve osteointegration. Osteointegration is the growing of the bone tissue into the implant which is porously structured for that purpose. Relative motion between implant and bone exceeding 100µm to 120µm will prevent bony in growth. It has been observed that if the implant is not well attached, softer tissues will fill the gap and cause partial or total failure of the operation. Implant displacements up to 3 cm have been observed. It has also been observed that the optimal osteointegration occurs during the first few weeks after the operation.

The task proposed is to monitor the displacements of an implant with a sensing system placed inside the pelvic girdle. This is to be done in laboratory conditions. Specified loads are then applied to the joint and the relative displacement observed. The results observed will be used to specify treatment conditions for the patients with the aim to raise the efficiency of the operation.

In order to measure these displacements, a Bone Implant Relative Displacement System (BIRDS) has been developed. The diameter of the device should not exceed 4 millimetres so that the mechanical behaviour of the host bone is altered as little as possible. Axial displacements of 150 µm and lateral displacements of 300 µm have to be acquired with a resolution of at least 10 µm.[37]

The BIRDS developed is based on a hybrid structure. The range covered is too high to be measured directly. A mechanical element acts as interface between a sensor-chip and the implant so as to transform and reduce the displacements. Different available sensor-chips were tested. The most promising results are obtained with a membrane pressure sensor using diffused piezo-resistors to measure the deformation of the membrane.

6.2 Principle

The approach chosen is to decouple the displacements and to transform them into forces. This is achieved using an elastic element, a spring. As shown in figure 57, the sensor consists of an carrier frame and a mass suspended by four beams. The beam thickness is 20 µm and contains the diffused piezo resistors. Between mass and frame a silicon nitride membrane 0.2 µm thick separates the upper and lower parts of the sensor, initially used in absolute pressure measurement [37].

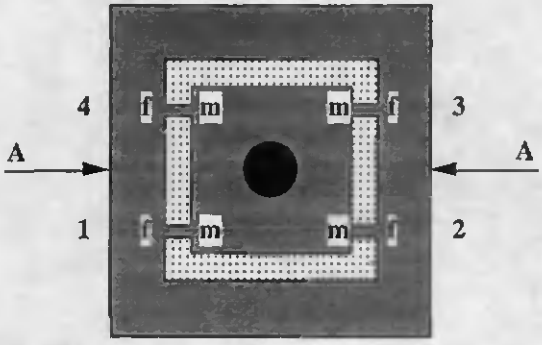

Figure 57 Top view of sensor chip

The sensor chip is attached to a pyrex glass. A 10 µm thick spacer ensures that the mass is free to move when submitted to forces.(see figure 58)

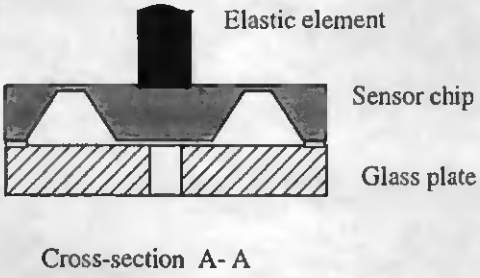

Figure 58 Cross-section view of sensor chip

The tip of the spring is interfaced with the implant. Relative displacements of the tip, called the primary displacements, are transformed into reaction forces or moments on chip level. This is represented in figure 59.

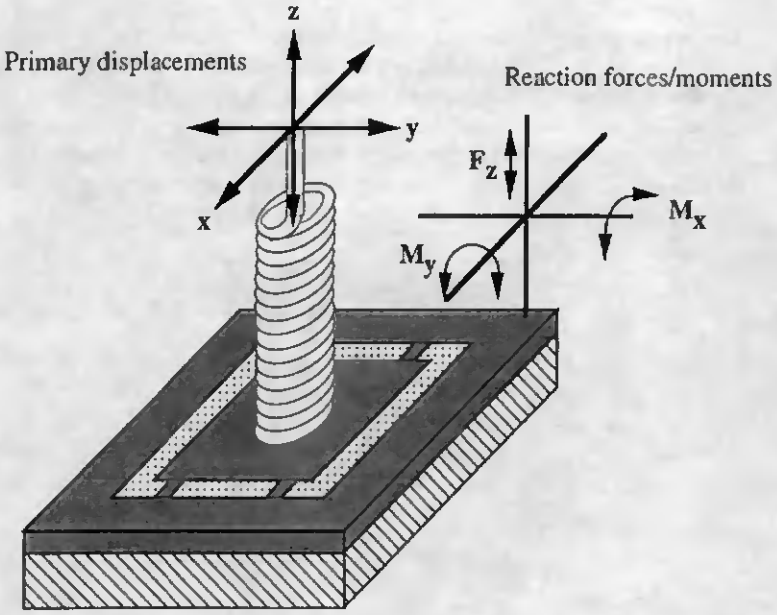

Figure 59 Force transformation principle

The determination of the spring characteristics was done by two successive iterations. First a strait spring wire was cemented perpendicularly to the upper surface on the sensor chip. This enabled the determination of the sensors range. Using the obtained measurements in x,y and z direction a wound spring was defined having the following characteristics:

$$k_Z = 100 \frac{N}{m}$$

and

$$k_X = k_Y = 5 \frac{N}{m}$$

The exterior shape of the spring is conical to minimise the risk of buckling when compressive force is applied in the z-direction. The sensor and spring are cemented to each other, and characterised. The whole device is accommodated in a cylindrical housing that in turn acts as an interface to the host bone.

6.3 **Testing and results**

By moving the end of the spring in x and y directions, moments M_X and M_Y are generated whereas a z displacement generates a force F_Z in the centre of the mass. The strain induced by these forces is measured by piezo-resistors. The position and orientation of these resistors are important to allow simple signal treatment. Figure 59 shows an orientation which allows independent changes of the resistors. The stress in the suspensions is tensile (-) or compressive (+), depending on the type of primary movement. The effects of independent primary displacements are shown in figure 60.

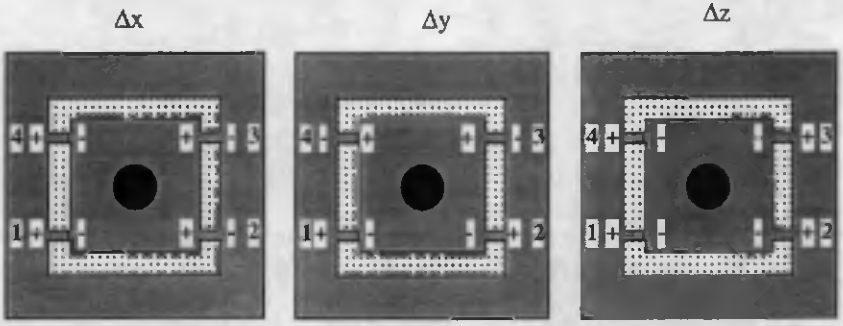

Figure 60 Effects of independent primary displacements.

Resistors 1 and 3 are place near the frame of the chip and resistors 2 and 4 near the mass. Table 6 shows the variations in resistance for positive primary displacements.

Table 6 Resistance change as function of displacements.

	ΔR for Δx	ΔR for Δy	ΔR for Δz
R_1 (frame)	+	+	+
R_2 (mass)	+	-	-
R_3 (frame)	-	-	+
R_4 (mass)	-	+	-

If the four resistance changes are independent, that is if the stress induced by a composed displacement is the sum of independent effects, we have a system of 4 equations having only three unknown.

The variations of resistance, proportional to the voltage drop over the Wheatstone bridge, due to the displacement "r" of the implant have a linear relationship. This can be expressed in form of a matrix $\mathcal{A}$. For reasons of symmetry, an additional parameter "c" is integrated giving the matrix a four by four dimension.

We have:

$$\begin{bmatrix} \Delta V_1 \\ \Delta V_2 \\ \Delta V_3 \\ \Delta V_4 \end{bmatrix} = \begin{bmatrix} \frac{\partial V_1}{\partial x} & \frac{\partial V_1}{\partial y} & \frac{\partial V_1}{\partial z} & \frac{\partial V_1}{\partial c} \\ \frac{\partial V_2}{\partial x} & \frac{\partial V_2}{\partial y} & \frac{\partial V_2}{\partial z} & \frac{\partial V_2}{\partial c} \\ \frac{\partial V_3}{\partial x} & \frac{\partial V_3}{\partial y} & \frac{\partial V_3}{\partial z} & \frac{\partial V_3}{\partial c} \\ \frac{\partial V_4}{\partial x} & \frac{\partial V_4}{\partial y} & \frac{\partial V_4}{\partial z} & \frac{\partial V_4}{\partial c} \end{bmatrix} \begin{bmatrix} \Delta x \\ \Delta y \\ \Delta z \\ \Delta c \end{bmatrix} \quad \text{or} \quad \Delta\vec{V} = \mathcal{A}\Delta\vec{r} \qquad (41)$$

To determine the matrix elements $\mathcal{A}_{ij}$, separate displacements in x, y and z direction are made. The four voltage changes are recorded and the sensitivity determined for every axis. This matrix is the calibration matrix and has to be determined for every sensor. When inverting the matrix, the displacement can be obtained by introducing the voltage variations observed. We have:

$$\Delta\vec{r} = \mathcal{A}^{-1}\,\Delta\vec{V} \qquad (42)$$

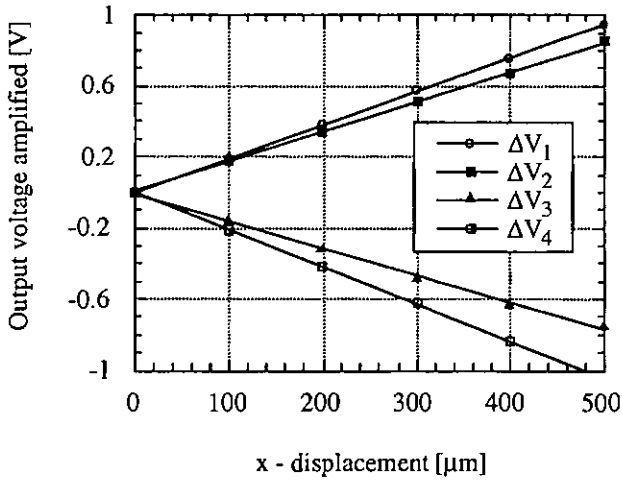

Figure 61 Sensor response to x - displacement

As shown in figure 61, voltage variations corresponding to a one axis displacement yield a linear signal amplified one thousand times. This has been repeated for all three axis. We have:

$$\begin{bmatrix} \Delta V_1 \\ \Delta V_2 \\ \Delta V_3 \\ \Delta V_4 \end{bmatrix} = \frac{1}{1000} \begin{bmatrix} 1.89 & 1.49 & 9.93 & 1000 \\ 1.72 & -1.01 & -9.29 & 1000 \\ -1.58 & -1.17 & 9.57 & 1000 \\ -2.09 & 1.26 & -9.93 & 1000 \end{bmatrix} \begin{bmatrix} \Delta x \\ \Delta y \\ \Delta z \\ \Delta c \end{bmatrix}$$

Matrix elements are expressed in Volts per micrometer. The "c" contribution is chosen to be 1. Inverting the matrix yields the system of equations for absolute displacement as a function of voltage variations. After eliminating the parameter "c" contribution we have:

$$\begin{bmatrix} \Delta x \\ \Delta y \\ \Delta z \end{bmatrix} = \begin{bmatrix} 122 & 152 & -130 & -145 \\ 213 & -194 & -210 & 192 \\ 23.3 & -28.2 & 28.5 & -23.6 \end{bmatrix} \begin{bmatrix} \Delta V_1 \\ \Delta V_2 \\ \Delta V_3 \\ \Delta V_4 \end{bmatrix} \qquad (43)$$

Verifications

Mounted on a test bench, controlled 3D-displacements were applied to a BIRDS. The output voltages of the four Wheatstone bridges were fed into equation (43) and the measured results compared with the applied displacement values. Some of the results obtained are shown in table 7.

Table 7 Comparison between set and measured displacements

Displacement axis	Set values [µm]	Measured values [µm]
Δx_1	250	220
Δy_1	-250	-260
Δz_1	-50	-44
Δx_2	-250	-220
Δy_2	250	230
Δz_2	-50	-49
Δx_3	-250	-230
Δy_3	-250	-260
Δz_3	-50	-55

It is to note that the displacement was achieved with a mechanical x,y,z-stage. The precision of the set displacements is therefore in the order of 5 to 10 µm. We can however say that the measured values correspond to the set value within about 10%. For large composite displacements, the cross-influence and the geometrical tolerances due to mounting and interfacing become more important and have an effect on the measurement precision.

6.4 Conclusion

Test are currently underway in medical laboratory conditions. If the results continue to be promising, the system will again go into development so as to optimise the reliability of the measurements and the reproducibility of the manufacturing sequence. This last point will include the integration of all or part of the measurement electronics on the sensor chip.

7. Outlook

This chapter gives examples of applications of the components presented earlier. It shows that hybrid micro systems can be used to solve various research or industrial problems.

7.1 Introduction

The devices and systems presented hereafter have been developed or are still under development in the Institute of Microtechnology, Neuchâtel, Switzerland. The goal of this chapter is to show the practical use of such devices.

7.2 Examples

The most striking example of a complet hybrid sytem using conventional mechanics, chemical sensing devices as well as fluid handling components is a miniature bioreactor developed for experimentation under micro-gravity conditions on board of the spacelab [25]. The bioreactor is shown in figure 62.

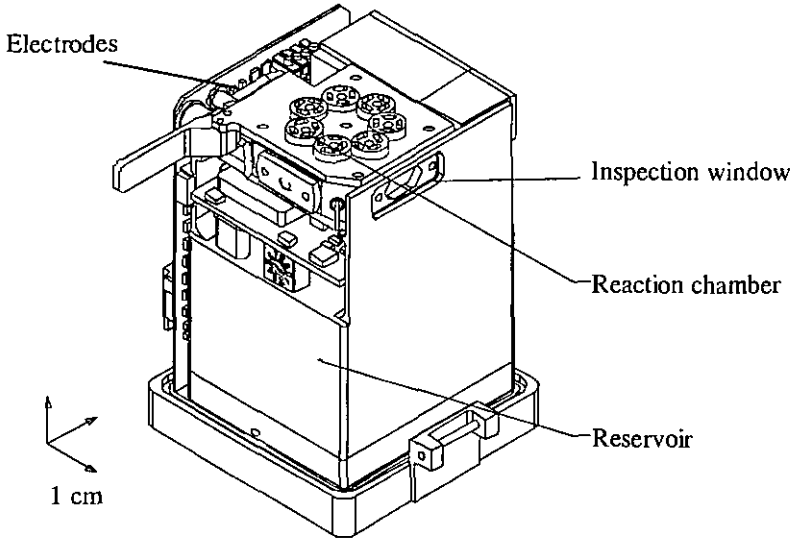

Figure 62 Space bioreactor

This experiment has been selected by the European Space Agency (ESA) for the IML-2 mission scheduled for summer 1994. This work was done in collaboration with MECANEX S.A., Nyon, Switzerland. Yeast cells are grown over a period of 9 days and various properties of the culture are monitored. The feeding of fresh nutritif medium is achieved by a micro pump identical to the one presented earlier. In fact this project was the driving motivation to develop the enhanced micro pump.

Another example is the flow rate sensor which is currently being tested as a single device by the technical University of Darmstadt, Germany. Their application consists in monitoring the production of cerebrospinal fluid in hydrocephalus patients. In this sickness, too much fluid is produced which causes an important increase in pressure inside the skull. The only means to relieve this phenomena is to implant a drain into the skull, equipped with a passive valve, allowing the excessive fluid to flow out of the skull back into the trunk of the body as can be seen in figure 63. The flow rate sensor is to be integrated to this drain in order to gain better understanding of the phenomena. This type of sensing was selected as the physical properties of the fluid are not altered.

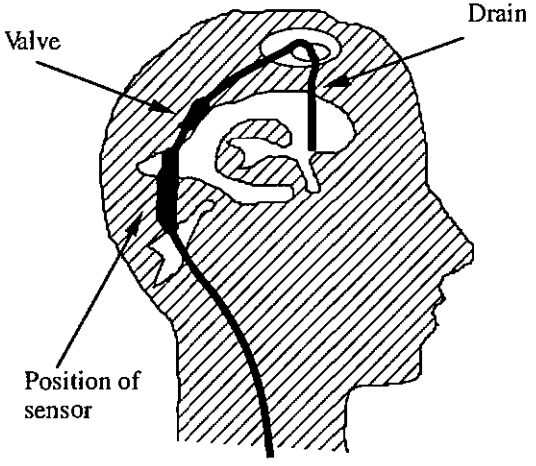

Figure 63 Fluid drain implant in human skull

The power and data transfer to and from the sensor are to be executed by telemetry. This is the most interesting potential application of the flow rate sensor.

Lastly, most recent contacts with Adidas Research Centre, Portland, USA, have given rise to an absolute 3-D force measurement based on the BIRDS presented in chapter 6. This system represented in figure 64 is developed with the objective to quantify the interactions between foot and shoe so as to optimise its design.

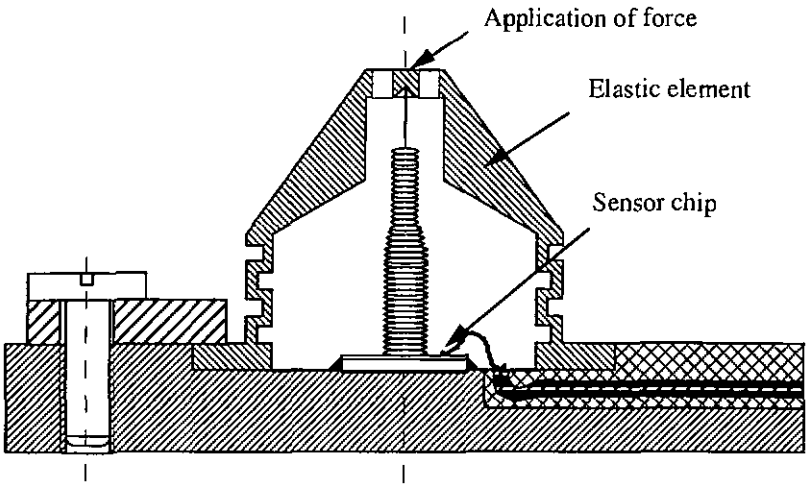

Figure 64 3-D force measurement system

Figure 64 is represented with a scale of 4:1. The Elastic element, made of titanium alloy, transforms the forces (up to 2000 Newton) into a displacement measured by a system identical to the BIRDS.

7.3 Conclusion

Three different applications of hybrid systems and discreet components have been shown. Their use is mainly found in small series and laboratory equipment. However, the torque sensor presented in chapter 5 is currently being put into industrial production.

8. Conclusion

The goal of this thesis was the development of a flow rate sensor and its integration to a micro pump in order to regulate the pump's output. This has been achieved. The project spin-offs described in the last three chapters have shown that hybridisation in micro systems is often a rapid solution to solve laboratory and in some cases industrial problems.

The flow rate sensor has been developed using available technologies. This confirms the utility of standardisation in the manufacturing processes to allow rapid transition from ideas on paper to functional prototypes.

Integrating the sensor to a micro pump and controlling the pump's output in a feed-back loop has allowed to maintain desired flow rate constant and un susceptible to changes in pressure. The limitation of the measurement set-up can be overcome by modifying the electrical components of the system.

The use of the flow sensor to measure force in a hybrid torque meter has given rise to a new product. The same approach has allowed measurement of 3-D displacement with the BIRDS device and 3-D force for an application in the shoe industry.

Acknowledgements

The co-operation, knowledge and experience of a number of persons has been a great help to me during the work on my thesis. I want to express my sincere gratitude to all the persons who contributed to this work.

Special thanks, I owe to:

Prof. N. F. de Rooij, for offering me the chance to write the thesis and for his continuous interest in this work;

Dr. B van der Schoot from the IMT, for the excellent collaboration and support throughout his project;

All my colleagues of the "group de Rooij" of the Institute of Microtechnology in particular:

M.-A. Gretillat, S. Jeanneret and L. Paratte for the collaboration on silicon technology and its applications;

P.-A. Clerc, for the collaboration on plasma etching technology and applications;

S. Pochon for valuable assistance in encapsulation and wire-bonding;

Further I thank Dr. P.-A. Mäusli form Mecanex and Dr. H. Hügli from the IMT for kindly agreeing to be examiners.

The present work has been done under a project of the Swiss Committee for the Promotion of Applied Scientific Research (CERS), with as industrial partner CIBA-GEIGY Ltd, Basel, Switzerland.

References

[1] B. H. van der Schoot, A. van den Berg, S. Jeanneret, N. F. de Rooij, "A Miniaturized Chemical Analysis System Using two Silicon Micro Pumps", Technical Digest, IEEE, Transducers'91. 1991, p. 789-791.

[2] E. Bassous, H.H. Taub, L. Kuhn "Ink Jet Printing Nozzle Arrays Etched in Silicon.", Appl. Phys. Lett. 31, 2, 1977, p. 135-137.

[3] T.S.J. Lammerink, N.R. Tas, M. Elwenspoek, J.H.J. Fluitman, "Micro-Liquid Flow Sensor.", Sensors & Actuators. A 37-38, 1993, p. 45-50.

[4] S.C. Terry, J.H. Jerman, J.B. Angell, "A Gas Chromatogrlphic Air Analyzer Fabricated on a Silicon Wafer.", IEEE Trans. Electron Devices. ED-26, 12, 1979, p. 1880- 1886.

[5] M.J. Zdeblick, P.W. Barth, J.A. Angell, "Microminiature Fluidic Amplifier.", Technical Digest, IEEE, Solid-state Sensor and Actuator Workshop. 1986.

[6] F.C.M. van de Pol, J. Branebjerg, "Micro Liquid-Handling Devices - A Review", Proceedings, Micro System Technologies 90. 1990, p. 799-805.

[7] A. Richter, K.A. Hoffmann, A. Plettner, H. Sandmaier, "The Electrohydrodynamic Micro Flow Meter.",Technical Digest, IEEE, Transducers'91. 1991, p. 935-938.

[8] M. Esashi, S Eoh, T. Matsuo, S. Choi, "The Fabrication of Integrated Mass Flow Controllers", Proc. 4th Int. Conf. Solid-State Sensors and Actuators (Transducer '87), Tokyo, Japan, 1987, p. 830-833.

[9] O. Tabata, H. Inagaki, I. Igarashi, "Monolithic pressure-flow sensor with Thermal isolation structure", Proc. 4th Int. Conf. Solid-State Sensors and Actuators (Transducer '87), Tokyo, Japan, 1987, p. 340-343.

[10] J. Branebjerg, O. Sondergard, N.G. Laursen, O. Leistiko, H. Soeberg, "A Micromachined Flow Sensor for Measuring Small Liquid Flows", Technical Digest, IEEE, Transducers'91. 1991, p. 41-44.

[11] R. W. Fox, A. T. McDonald, "Introduction to fluid Mechanics", John Wiley ans Sons, 1990.

[12] B. Hälg, "A Silicon Pressure Sensor with an Interferometrical Readout",, IEEE, Transducers'91. 1991, p. 682-684.

[13] M.A. Schmidt, R.T. Howe, S.D. Senturia, J.H. Haritonidis, "A Micromachined Floating-Element Shear Sensor", Technical Digest, IEEE, Transducers'87. 1987, p. 383-386.

[14] T. Tschan, "Simulation, Design and Characterization of a Silicon Piezoresistive Accelerometer, Fabricated by a Bipolar-Compatible Industrial Process", Dissertation, University of Neuchâtel, Switzerland, 1992.

[15] L. Field, R. White, A. Pisano, "Fluid-Powered Rotary Gears and Micro-Flow Channels", IEEE, Transducers'91. 1991, p. 1033-1036.

[16] P. Bley, J. Göttert, M. Harmening, M. Himmelhaus, W. Menz, J. Mohr, C. Müller, U. Wallrabe, "The Liga Process for the Fabrication of Micromechanical and Microoptical Components", Proceedings, Micro System Technologies 91. 1991, p. 302-314.

[17] J. G. Smits, "Piezoelectric micropump for peristaltic fluid displacements", NL patent 8302860, 1985.

[18] H.T.G. van Lintel, F.C.M. van de Pol, S. Bouwstra, "A Piezoelectric Micropump Based on Micromachining of Silicon.", Sensors & Actuators. 15, 2, 1988, p. 153-167.

[19] H.T.C van Lintel, F.C.M. van de Pol, S. Bouwstra, "A Micro Pump Based on Micromachining of Silicon", Proceedings, Eurosensor 1. 1987, p. 20-21.

[20] R Zengerle, M Richter, F Brosinger, A Richter, H. Sandmaier, "Performance Simulation of Microminiaturized Membrane Pumps.', Technical Digest, IEEE, Transducers'93. 1993, p. 106-109.

[21] H. Matsumoto, J.E. Colgate, "Preliminary Investigation of Micropumping Based On Electrical Control of Interfacial Tension.", Proceedings, IEEE, MEMS'90. 1990, p. 105-110.

[22] J G. Smits, "Piezoelectric Micropump with three valves working peristaltically.". Sensors & Actuators. A, 21-23, 1990, p. 203-206.

[23] R. Zengerle, A. Richter, H. Sandmaier, "A Micro Membrane Pump with Electrostatic Actuation.", Proceedings, MEMS'92. 1992, p. 19-24.

[24] "Procédé de fabrication d'un dispositif micro-usiné déstiné à contenir ou à véhiculer un fluide", Patent application France No 93 06281, May 1993.

[25] Ph. Arquint, B. Bechler, A. Cogoli, N. F. de Rooij, V. Gass, F. K. Gmünder, M.-T. Ivorra, S. Jeanneret, G. Lorenzi, P.-A. Mäusli, B. H. van der Schoot, I. Walther, "Microsystem technology for biological experiments in space; development of a miniature bioreactor", Technical Digest, IEEE, Transducers'93. 1993, p. 921-923.

[26] V. Gass, B.H. van der Schoot, N.F. de Rooij, "Nanofluid handling by micro-flow-sensor based on drag force measurements.R, Proceedings, MEMS'93. 1993, p. 167-172.

[27] P. Gravensen, J. Branebjerg, O. Søndergård Jensen, "Microfluidics- a review", J. Micromech. Microeng. 3 (1993), p. 168-182.

[28] B. Kloeck, "Design, Fabrication and Characterization of Piezoresistive Pressure Sensors, Including the Study of Electrochemical Etch-stop", Dissertation, University of Neuchâtel, Switzerland, 1989.

[29] M. Boillat, "Multisensor project, CERS 2488.1", Internal Progress Report, University of Neuchâtel, Switzerland, March 17, 1994.

[30] V. Gass. B.H. van der Schoot, S. Jeanneret, N.F. de Rooij, "Integrated Flow-Regulated Silicon Micropump.", Technical Digest, IEEE, Transducers'93. 1993, p. 1048-1051.

[31] V. Gass, B.H. van der Schoot, S. Jeanneret, N.F. de Rooij, "Micro liquid handling using a flow-regulated silicon micropump", J.Micromech. Microeng. 3 - 4,. 1993, p. 214- 215.

[32] F. H. Raven, "Automatic Control Engineering", McGraw-Hill, 1991.

[33] A. Roch, E. Wild, "Cours d'automatique", Ecole Polytechnique Fédérale de Lausanne, Ecublens, 1985, p. 130-133"

[34] Y. Mikuriya, K. Matsuzaki, T. Matsuo, "Fabrication and Evaluation of Micromotors", IARP Workshop on Microsystems and Robotics, 15-16 juin 1993, Karlsruhe, Germany.

[35] V. Gass, B. H. van der Schoot, S. Jeanneret, N.F. de Rooij, "Micro-Torque sensor based on differential Force measurement", Proceedings IEEE MEMS workshop, Oiso, Japan, jan. 1994, pp. 241-244.

[36] G.-A. Racine, R. Luthier, N.F. de Rooij, "Hybrid Ultrasonic Micromachined Motors", Proceedings IEEE MEMS workshop, Fort Lauderdale, FL, Feb. 1993, pp. 128-132.

[37] V.L. Spiering, V. Gass, S. Jeanneret, N.F. de Rooij, "A 3-Dimensional Relative Displacement Sensor for Biomedical Applications", Proceedings Sensor Technology National Conference, Enschede, NL, feb. 1994, p. 31-35"

[38] A. van der Wiel, N. F. de Rooij, "Dévelopment de capteurs de débit pour applications biomédicales", Final Report, CERS 2023.2, University of Neuchâtel, Switzerland, March 30, 1993.

[39] A. van der Wiel, C. Linder, N. F. de Rooij, "A liquid velocity sensor based on the hot-wire principle.". Sensors & Actuators. A, 37-38, 1993, p. 693-697.